Biological impact of nanodiamond particles – label free, high-resolution methods for nanotoxicity assessment.

Dipesh Khanal[1], Fan Zhang[2], Yang Song[3], Herman Hau[1], Archana Gautam[4], Seiji Yamaguchi[5], Jamie Uertz[6], Stewart Mills[6], Alexey Kondyurin[7], Jonathan C. Knowles[8,9,10], George Georgiou[8], Iqbal Ramzan[1], Weidong Cai[11], Kee Woei Ng[4], Wojciech Chrzanowski[1*]

*Correspondence: wojciech.chrzanowski@sydney.edu.au

Full list of author information is available at the end of manuscript.

Abstract

Current methods for the assessment of nanoparticle safety that are based on 2D cell culture models and fluorescence-based assays, show limited sensitivity and they lack biomimicry. Consequently, the health risks associated with the use of many nanoparticles have not yet been established. There is a need to develop *in vitro* models that mimic physiology more accurately and enable high throughput assessment. There is also a need to set up new assay that offer high sensitivity and are label-free. Here we developed 'mini-liver' models using scaffold-free bioprinting and used these models together with label-free nanoscale techniques for the assessment of toxicity of nanodiamond produced by laser-assisted technology. Results showed that NDs induced cytotoxicity in a concentration and exposure-time dependent manner. The loss of cell function was confirmed by increased cell stiffness, decreased cell membrane barrier integrity and reduced cells mobility. We further showed that NDs elevated the production of reactive oxygen species and reduced cell viability. Our approach that combined mini-liver models with label-free high-resolution techniques showed improved sensitivity in toxicity assessment. Notably, this approach allowed for label-free semi-high throughput measurements of nanoparticle-cell interactions thus could be considered as a complementary approach to currently used methods.

Keywords: nanodiamond, nanosafety, atomic force microscopy, 3D liver model, mechanobiology, nanomechanics, holotomography.

Introduction

Engineered nanoparticles became an integral component of cosmetics, food, biosensors and therapeutics. Nanoparticles are often considered to be 'safe', which is defined as 'not causing substantial harm'. However, the negative impact of nanoparticles on human health and the environment has been demonstrated in increasing number of reports (Bettini, et al., 2017, Peng, et al., 2019, Setyawati, et al., 2013, Setyawati, et al., 2017, Yamashita, et al., 2011, Pinget, et al., 2019). Among different classes of engineered nanoparticles, nanodiamonds (NDs) have gained significant attention for drug delivery (Alhaddad, et al., 2011, Li, et al., 2010, Wang, et al., 2013, Zhao, et al., 2014) and bioimaging (Zhang, et al., 2012, Luo, et al., 2016, Brady, et al., 2015, Manus, et al., 2009, Chao, et al., 2007, Lee, et al., 2017). NDs can be manufactured using different methods such as detonation, high-pressure high-temperature synthesis (HPHT) (Boudou, et al., 2009), laser assisted technology (Baidakova, et al., 2013) and plasma assisted chemical vapor deposition. Each method results in NDs of varying structure, size and purity. As such, their safety cannot be generalised without the assurance that the different manufacturing processes induce different physical-chemical properties and thus different biological activity.

Some studies have suggested that NDs are biocompatible and non-cytotoxic (Moche, et al., 2017, Paget, et al., 2014), while Krüger *et al.* and Mytych *et al.* showed that HPHT NDs is cytotoxic (Krüger, 2006, Mytych, et al., 2014). Through *in vivo* experiments Yuan *et al.* showed that NDs were stable, non-biodegradable and retained in the body for 28 days (experiment end point) (Yuan, et al., 2009). A study by Chu has suggested that the 'coarse' edges of NDs, allow them to escape the endosomes and reach cytoplasm of cells, which may lead to toxicity (Chu, et al., 2015). Hence, the poorly understood interactions of

nanodiamonds with body fluids, cell and tissues, its long-term stability and non-degradability have raised major safety concerns.

With the emergence of conflicting reports, it is clear that there are flaws in the current methodologies used for nanotoxicity assessment. Some of the major limitations include the lack of biomimicry in the *in vitro* models, the lack of long term nanoparticle exposure studies, the lack of high-throughput in majority of methods used for nanotoxicity assessment and the limited spatial resolution of conventional methodologies to evaluate the impact of nanoparticles on cells or tissues. Therefore, it is critical to reassess the safety of existing and emerging classes of nanoparticles before clinical or commercial use. However, achieving this goal will require an update to the regulatory framework and protocols used for nanosafety assessment.

2D vs 3D models for toxicity assessment

Traditionally, 2D cell culture models have been used for assessing nanoparticle safety. Although these models do not mimic *in vivo* environment (Lee, et al., 2009, Chia, et al., 2015), they remain in use for chemical safety assessment. 3D tissue-like models have been found to bridge the gap between *in vitro* 2D cell culture models and animal models (Yamada and Cukierman, 2007). 3D models replicate the complex multicellular networks that support the physiological exchange of nutrients, promote the formation of extracellular matrixes and facilitate the retention of cellular polarity for tissue organization (Daquinag, et al., 2012). Thus, 3D models are more effective than 2D cell cultures in investigating processes such as the translocation of nanoparticles through cellular layers. Additionally, 3D models can be prepared in a configuration that allows for high-throughput

measurements to complement other high-content assessment methods (Collins, et al., 2017).

Characterization and assessment methods of toxicity

The cell cytoskeleton maintains the structural and mechanical integrity of the cell (Cai, et al., 2010) and plays a key role in signaling pathways also known as mechanical transduction (Haghi, et al., 2015). Changes in cytoskeletal structure regulate the function and mechanical properties of cells (Head, et al., 2014). The mechanical properties of cells are therefore considered as a biomarker of diseases and patho/physiological processes (Cross, et al., 2007, Li, et al., 2012). Hence, by measuring mechanical properties of cells we are able to assess the toxicity of nanoparticles.

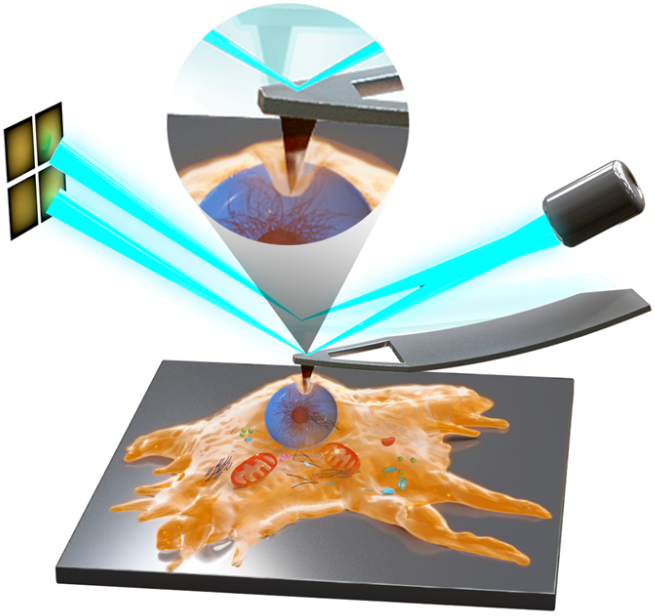

Fig.1: Schematics for atomic force microscopy based nanoindentation technique for biomechanical measurement of cell.

One of the techniques used to measure the mechanical properties of cells is atomic force microscopy (**Fig. 1**). Due to its high resolution, ability for correlative label-free imaging and mapping of mechanical properties (Kirmizis and Logothetidis, 2010, Butt, et al., 2005, Webb, et al., 2011), AFM is well-placed for testing the biological impact of nanoparticle on cells/tissues.

Conventional techniques such as Fourier transform infrared spectroscopy, Raman spectroscopy used for nanotoxicity assessment have limited spatial resolution (micron level), which makes them suitable only for 'bulk' measurements. Conventional

nanotoxicity assays may also utilize fluorescent probes/dyes (Ong, et al., 2014). Since nanoparticles can interact with dyes, the results may be biased (Ong, et al., 2014). Therefore, it is critical to introduce new label-free techniques, which can characterize interactions of individual nanoparticles and cells at nano levels without the need for expensive dyes.

To address the aforementioned limitations, we first developed 'mini-livers' (3D liver model) using magnetic levitation and bioprinting, which allowed for high throughput assessment of nanoparticles toxicity. Next, we used an array of label-free methods including real time imaging, impedance spectroscopy and atomic force microscopy (force-volume mechanical properties measurements), to determine the toxicity of nanodiamond. The internalization, aggregation and accumulation of NDs in cells were measured using 3D holotomography, dark field hyperspectral imaging and scanning electron microscopy. For control experiments, we used 2D cell culture models and measured cell growth, quantified DNA and reactive oxygen species (ROS) production as measures of cytotoxicity.

The work presented here is significant because it provided a new approach for a comprehensive assessment of nanoparticle toxicity using nanoscale-resolution label-free methodologies and also demonstrated that 3D cell culture model – 'mini-livers' – were effective in rapid and semi high-throughput assessment of toxicity. Taken together, methodological advances presented here formed a framework for label-free, high-sensitivity nanotoxicity assessment. Our approach complements traditional methodologies and improves their sensitivity for the assessment of impact of nanoparticles on health.

Materials and Methods

Nanodiamond particle preparation and physico-chemical characterization

Nanodiamond particles (NDs) with nominal size 5 nm produced by laser-assisted technology (Ray Techniques Ltd., Israel) were sonicated in sterile deionized water (DI) at a concentration of 1 mg·mL^{-1} (DI) for 30 min at 60% amplitude using an ultrasonic probe. ND dispersions were UV sterilized and then characterized using atomic force microscopy (AFM), transmission electron microscopy (TEM), nanoparticle tracking analysis (NTA) and X-ray diffractometry (XRD) to ascertain nanoparticle size, shape, crystallographic structure and morphology. Surface chemical composition was investigated using Fourier transform infrared spectrophotometry (FTIR) and X-ray photoelectron spectroscopy (XPS).

Atomic Force Microscopy

ND were immobilized on a mica disc functionalized with 0.1% poly-L-lysine and scanned using AFM (Multimode VIII, Bruker, UK) in tapping mode at 0.5 Hz scan rate, using ultrasharp silicone tip (AppNano, ACTA-SS-10; resonance frequency 300 kHz and spring constant 37 Nm^{-1}).

Transmission electron microscopy

ND dispersions were drop casted onto carbon-coated copper grids (Ted Pella Inc., USA) and dried in desiccator before imaging. Images were acquired using TEM (Carl Zeiss Libra 120) with an accelerating voltage of 120 kV, magnification 80,000×.

Nanoparticle tracking analysis (NTA)

NDs were diluted to 5 µg·mL^{-1} in cell culture medium (see cell based assays) and vortexed for 5 minutes prior to evaluation for size distribution on a Nanosight NS300 (Malvern, UK)

at 488 nm. Measurements were performed in triplicates; see supplemental materials for full protocol.

X-ray diffractometry (XRD)

XRD of NDs was performed on a D8 Advance Bruker diffractometer (Bruker, UK) in a flat plate geometry using Ni-filtered Cu Kα radiation and a Bruker Lynx eye detector. X-ray diffraction patterns were collected from 10 to 100 2θ with a step size of 0.02° and a count time of 0.1s.

Fourier transform infrared spectrophotometry (FTIR)

FTIR spectra were recorded by the attenuated total reflectance (ATR) technique using a FTIR7000 series spectrometer (Digilab, USA) with Germanium ATR crystal of 45 ° incident angle and globar source of IR irradiation. Absorbance spectra were recorded in mid IR (infrared) range from 4000 to 400 cm^{-1}, taking average of 500 scans with a resolution of 4 cm^{-1}.

X-ray photoelectron spectroscopy (XPS)

Elemental composition of NDs was analyzed using XPS (PHI 5000 Versaprobe II, Japan) using an Al-Kα monochromator X-ray source. Survey scan was acquired at 100 eV pass energy between 0 and 1400 eV. High resolution spectra for carbon, oxygen and nitrogen were collected at 20 eV pass energy. The elemental composition was calculated from the high-resolution spectra using CasaXPS.

Cell based assays

Rat hepatoma cells (Fao), which stably express a large set of functions specific to hepatocytes, including secretion of serum proteins and synthesis of hepatic neonatal enzymes, were used in this study. They have also been validated in previous studies on

liver toxicity (Chaya, et al., 1997, Cassio and Weiss, 1979, Deschatrette, et al., 1985). Fao cells were cultured in Dulbecco's Modified Eagle's Medium (DMEM) supplemented with 4.5 g/L D-glucose, 2 mM L-glutamine (Sigma-Aldrich, Australia), 1% Pen-Strep (Gibco, ThermoFisher SCIENTIFIC, Australia) and 10% Fetal Bovine Serum (Sera Laboratories). Fao cells were used to prepare both two-dimensional (2D) and 'mini-livers' – three-dimensional (3D) liver cell culture models. Cytotoxicity of NDs was determined by measuring ROS level, metabolic dehydrogenase activity, DNA concentration, impedance measurement and changes to the cytoskeleton organization. Cellular uptake and localization of NDs was determined using label-free methods: holotomography, dark field hyperspectral imaging, scanning electron microscopy (SEM) and AFM.

Quantification of ROS

Fao cells were seeded in 96-well white walled plates (1×10^4 cells/100μL) and incubated overnight for attachment. The cells were treated for 24 h with preconditioned media containing NDs at concentrations 10, 25, 50, and 100 $\mu g \cdot mL^{-1}$. Menandione (20 μM) was used as a positive control. The production of ROS was measured using the ROS-Glo™ H_2O_2 Assay (Promega, Australia). As ROS generated during exposure is short lived, ND treatment was limited to 24 h.

Real-time cytotoxicity assay (RTCA)

Cells were seeded at a density of 2,000 cells/250 μL per well. Cell attachment was monitored using impedance measurement on an xCELLigence instrument (Roche, Germany). A stabilized impedance value indicated cell attachment (approximately 20 h post seeding). ND preconditioned media (2.5, 5, 10, 15 and 25 $\mu g \cdot mL^{-1}$) was added to wells and impedance measurements were performed every 15 min for 126 h. Impedance

measurements were also conducted for 168 h. However, significant differences in cell membrane integrity were observed within 126 h of exposure. At day 7, cells were over confluent and started detaching from the electrodes. Thus, the results obtained only up to 126 h were more representative of true proliferation of the cells and were reported below. Changes in electrical impedance were expressed as a dimensionless cell index value, obtained from the relative impedance changes corresponding to cellular coverage of the electrode sensors present in the wells. Before the cells were treated with nanodiamond, all impedance values were normalised to the values obtained from control cells (cells cultured in media only) at the time of exposure.

Cell viability assays

Cell viability was measured using CCK-8 assay (Dojindo Molecular Technologies Inc., Japan) which corresponds to WST-8 tetrazolium salt to assess mitochondrial dehydrogenase activity. Fao cells were seeded at a density of 2000 cells/well on 96-well plates and were allowed to attach overnight. Media was aspirated and replaced with ND-conditioned media containing 10, 25, 50 and 100 $\mu g \cdot mL^{-1}$ of NDs. At each predetermined time point (days 2, 4 and 7), cells were washed with PBS once and 100 µL of fresh media containing 10% CCK-8 reagent was added to each well. After three hours of incubation in the dark, the media was transferred to a new 96 well plate, and the optical density (OD) of each well was measured using a microplate reader at 450 nm (Victor x4 multilabel plate reader, Perkin Elmer, USA).

For DNA quantification, media was removed at day 2, 4 and 7 and each well was washed with PBS once followed by addition of 75 µL of CyQUANT NF® assay dye reaction mix (ThermoFisher Scientific, Australia). Plates were incubated in the dark for 45 min before

measuring fluorescence at excitation and emission wavelengths of 485 and 535 nm respectively using microplate reader (Victor X4, multilabel plate reader, Perkin Elmer, USA).

Cytotoxicity of ND in 3D mini-liver model

The effect of NDs on cell growth and function in a 3D mini-liver model was quantified using ring closure and dot assays following previously published methodology (Khanal, et al., 2017, Hau, et al., 2016, Timm, et al., 2013, Tseng, et al., 2015). In brief, cells were cultured overnight with magnetic nanoparticles (NanoShuttle−PL; Greiner Bio-One, USA) at a concentration of 8 μL/cm^2. After trypsinization, magnetized cells were levitated overnight using magnetic drives to form a 'cluster' of cells, which were then bioprinted in the shape of rings (2 × 10^5 cells per ring) and spheroids (1 × 10^5 cells per spheroid) using a set of magnetic drives. Mini-liver models in a form of rings and spheroids were treated with NDs at a concentration of 10, 25, 50 and 100 μg·mL^{-1} (**Fig. S5 and S6**). Both internal and external diameters were monitored in real-time for 48 h. Based on recorded images, the percentage rate of diameter and area change was calculated using Cytox® software, a custom-built software to estimate IC_{50} concentrations of NDs. See supplemental materials for full protocol and analysis.

Nanoparticle uptake and visualization

3D holotomography

Fao cells were seeded (5 × 10^4 cells) onto plasma treated glass bottom dishes (35 mm, Ibidi®, Denmark) and allowed to attach overnight. Media was replaced with ND preconditioned media at concentrations of 10, 25, 50 and 100 μg· mL^{-1}. Cells were exposed to NDs for up to 7 days and ND uptake and localization was determined after 2 and 7 days

using a 3D CellExplorer (NanoLive, Switzerland). The images were analyzed with STEVE® software (NanoLive, Switzerland).

Dark field hyperspectral imaging

Plasma treated glass coverslips were individually transferred to 6-well plate and seeded with 2.5×10^4 Fao cells. After overnight culture that allowed cells to attach, media was replaced with ND preconditioned media at concentrations of 10 and 25 $\mu g \cdot mL^{-1}$. Cells were exposed to NDs for up to 7 days and dark field hyperspectral imaging was done using CytoViva microscope (CytoViva, USA); see supplemental materials for full protocol.

SEM

Fao cells were treated with ND preconditioned media (25 $\mu g \cdot mL^{-1}$) for 24 h to allow ND internalization. Treated cells were washed, harvested, fixed, dehydrated and embedded in Spurr's resin (ProScitech, Australia) to obtain microtomed ultrathin (70 nm) sections for SEM imaging, using formvar coated TEM grids. SEM images were captured using a Sigma VP Zeiss field emission SEM in Gatan back scattered mode, maintaining a working distance of 5.1 mm with an electronic high-tension value of 1.60 kV. See supplemental materials for full protocol.

AFM imaging

Fao cells treated with NDs were imaged using a nanoIR (AnasysInstruments, USA), using silicon nitride cantilever probes with a nominal spring constant of 40 Nm^{-1} (EXT125, AppNano, Mountain View, CA) operating in tapping mode at a scan rate of 0.3 Hz.

Effect of nanodiamond on cytoskeleton

Cytoskeleton organization (actin fiber network) was analyzed through fluorescent imaging of phalloidin (f-actin)-stained samples using inverted fluorescent microscope (Nikon

TE2000-U, Japan). See supplemental materials for full protocol.

Fao cell morphology and stiffness measurements

To investigate the influence of NDs on cell stiffness, cell mechanical properties were measured using Molecular Force Probe (MF3D-Bio, Asylum Research, USA) operating in force-volume mode. See supplemental materials for full protocol.

Statistical analysis

All statistical analysis was carried out using GraphPad Prism software. Results were statistically compared using Student's t test, one way ANOVA and two way ANOVA with Tukeys multiple comparison test). Statistical significance was established at $p < 0.05$.

Results

Physico-chemical characterization

The XRD diffraction pattern for NDs had a two diffraction maxima at 2θ of 43.9 and 75.4, which correspond to diamond (Baidakova, et al., 2013). The average crystal size of the NDs was 5 nm based on the Scherrer formula (**Fig. 2a**).

Bulk chemical analysis (FTIR) revealed peaks at 1107 cm^{-1}, 1177 cm^{-1}, and 1256 cm^{-1}, which are typical for ND and associated with stretching vibration of C–O group (Baidakova, et al., 2013). Additionally, we observed low intensity peaks at 1384 cm^{-1} and 1436 cm^{-1} that corresponded to aceto-group and C–H (SP_3) bending vibration. Aceto-groups are likely to be related to the manufacturing process of NDs and they stabilize NDs structure (Mochalin, et al., 2012). Furthermore, peak at 1760 cm^{-1} (C=O) confirmed partial oxidation of NDs, while peaks at 1630 cm^{-1} (bending vibration) and 3400 cm^{-1} (O-H stretching vibration) corresponded to adsorbed water (Khanal, et al., 2016).

Nanoscale imaging and particle size analysis (**Fig. 2c, d**) showed that NDs were partly agglomerated and the size of individual particles was between 3-5 nm, while the average size of ND aggregates was between 22 and 233 nm (**Fig. 2e**). ND particles were negatively charged with a zeta potential of -24.2 mV.

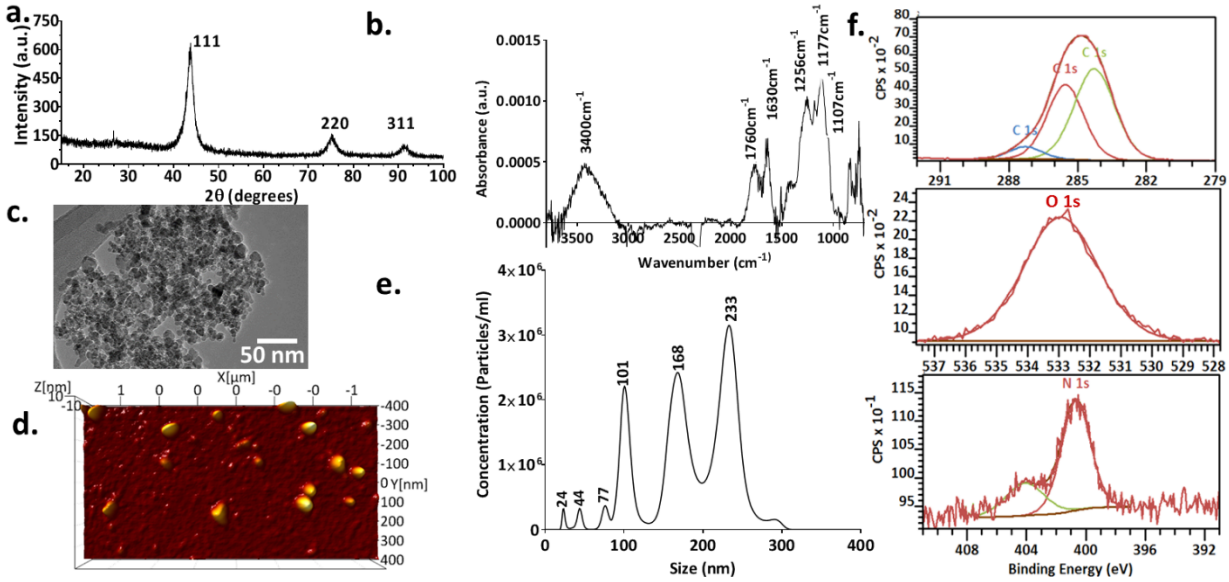

Fig.2: Physicochemical characterization of nanodiamond particles (NDs). (a) XRD graph showing key diamond peaks at 2θ of 111, 220, and 311. (b) FTIR spectra collected from the bulk of NDs indicated the presence of key diamond peaks in the region of 1117−1256 cm^{-1}. (c) TEM image of NDs (d) AFM height image of NDs. (e) Nanoparticle tracking analysis confirmed the presence of individual and aggregated NDs (f) XPS spectra collected from NDs showed peaks related to carbon, oxygen, and nitrogen.

Elemental analysis of NDs revealed the presence of three elements: carbon (C 1s), oxygen (O 1s) and nitrogen (N 1s). Deconvolution of the carbon (C 1s) spectra showed three characteristic peaks attributed to carbon in sp2 (hybridized carbon species; E_B = 283.95 eV), carbon in sp3 hybridization (diamond; E_B = 284.96 eV), and oxygen-containing groups (C−O; E_B = 286.23 eV) (**Fig. 2f**) (Xie, et al., 2010). Deconvolution of the oxygen (O 1s) peak evidenced peak associated with (C−O−C) and water adsorbed to the ND surface (E_B = 532.9 eV). The presence of oxygen (8%) in NDs confirmed the partial oxidation of NDs. Additionally, a small amount of nitrogen (1.7%) was detected on ND surface. Nitrogen spectra had two main peaks that correspond to N-C (E_B = 400.6 eV) and

N_2 (E_B = 404.1 eV). Nitrogen at the concentration up to 3% is a common impurity found in ND (Mochalin, et al., 2012).

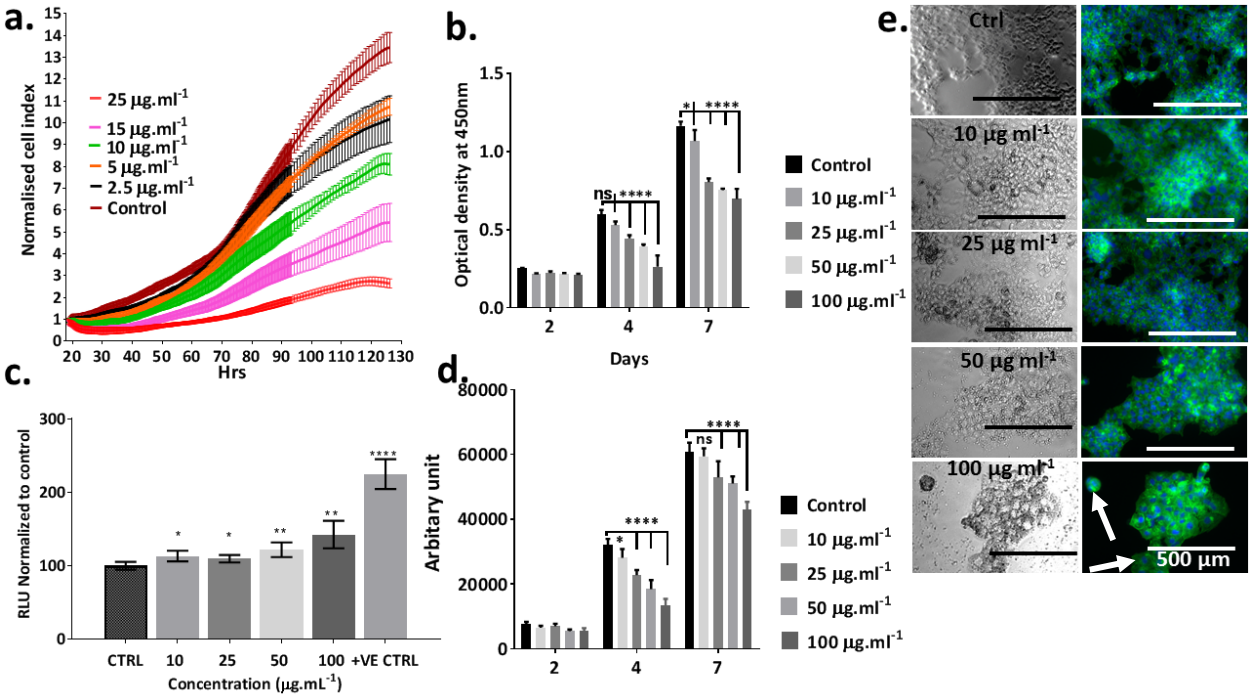

Fig. 3: Viability measurements of cells exposed to nanodiamond. (a) Real time impedance measurement of ND treated cells. (b) WST-8 assay of cells exposed to NDs. (c) Reactive oxygen species assay (ROS). (d) DNA quantification assay. (e) Phase contrast images along with the corresponding immunostaining images of cells with actin (phalloidin) and nucleus (DAPI) staining of cells exposed to NDs at day 7. All data presented as mean±SD, n=3. P<0.05 two way ANOVA with Tukeys multiple comparison (WST-8 and DNA quantification assay, P<0.05 students t-test (ROS assay).

Real time cytotoxicity assay

The impedance measurements showed that NDs decreased cell growth rate after 48 h of exposure when compared to control, untreated cells. Notably, after 90 h, cell impedance decreased substantially for cells treated with NDs and the drop was concentration-dependent (**Fig. 3a**). After 126 h, the cell growth dropped by approximately 80, 60 and 40% respectively for samples treated with ND at the concentration of 25, 15, and 10 µg mL^{-1} (**Fig. 3a**). These results evidenced that ND substantially reduced the barrier integrity of cells and/or inhibited cell proliferation.

Cell viability assays

Both the WST-8 and DNA quantification assay demonstrated that the NDs did not induce major changes to the amount of DNA and mitochondrial dehydrogenase activity for up to 48 h (**Fig. 3 a, b, c and d**). However, after 48 h mitochondrial dehydrogenase activity and DNA content sharply declined for samples treated with ND at and above 25 $\mu g \cdot mL^{-1}$, and the drop was concentration and exposure time dependent (**Fig. 3b & d**). At day 7, the metabolic dehydrogenase activity was reduced to 30%, 36% and 41% for sampled treated with 25, 50 and 100 $\mu g \cdot mL^{-1}$ of NDs when compared to control samples. These results indicates that prolonged exposure of cells to NDs, decreased the mitochondrial dehydrogenase activity of cells and led to cell death as evidenced by substantial decrease in DNA content; $P < 0.0001$. The decrease in cell viability was further confirmed by phase contrast imaging (**Fig. 3e**).

Furthermore, we showed that NDs distorted the organization of cytoskeleton, which was poorly defined and randomly distributed for all ND treated cells. In addition, ND treated cells were larger than control cells, indicating giant cell formation (**Fig. 3e, white arrows**).

Measurement of reactive oxygen species

Cells treated with 10, 25, 50 and 100 $\mu g \cdot mL^{-1}$ of NDs displayed a 13%, 9%, 22% and 40% increase in ROS over untreated cells **(Fig. 3c, $p<0.05$),** as measured using ROS-Glo™ H_2O_2 assay. The increase in ROS was ND concentration-dependent for concentrations ≥ 25 $\mu g\ mL^{-1}$. Since increased ROS production corresponds to oxidative stress, these results confirmed that NDs induce cell injury upon internalization.

3D semi-high throughput ring closure and dot assay for toxicity assessment

The rate of closure of both mini-organ models (rings and dots) were used to determine the cytotoxicity of NDs (Timm, et al., 2013, Tseng, et al., 2015). Changes to the diameters and surface areas of both mini-organ models showed concentration-dependent cytotoxicity. Notably, cytotoxicity was detected within the first 48 h, which suggested higher sensitivity of mini-organ models than 2D culture models. For untreated mini-organ models, the internal diameter of the ring was reduced to almost zero (fully enclosed ring). In contrast, internal ring remained open for mini-organ models treated with ND (**Fig. 4 a, b**).

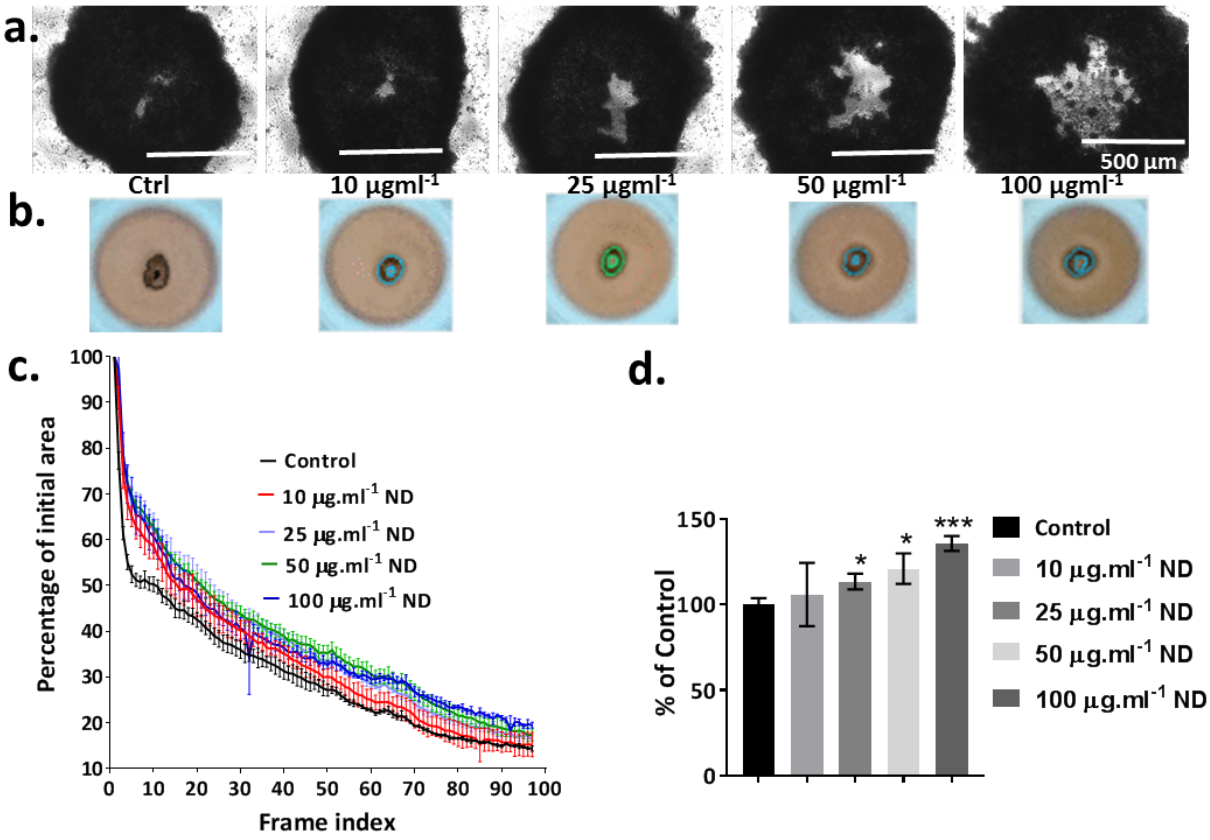

Fig. 4: 3D-ring closure assay. (a) Phase contrast image of the rings exposed to NDs, higher concentrations of ND led to decreased cell migration and cell functionality. (b) Corresponding images of the rings along with the outer contour acquired by the mobile device and analyzed using a custom built Cytox® software. (c) Graph showing the rate of decrease of the ring's area over a period of 48 h (each image frame was acquired at 30 minutes interval). (d) Comparison of ring area at the experiment end point. All data presented as mean±SD, n=3;P<0.05 students t-test.

The closure of the ring was statistically significant for samples treated with NDs at and

above the concentration of 25 μg·mL^{-1} (**Fig. 4 a, b**).

Importantly, the surface area of the rings exposed to NDs was substantially greater (20% and 35% for 50 and 100 μg mL^{-1}) than that of the untreated rings (**Fig. 4 c and d**).

Similarly, the rate of the spheroid shrinkage, which is a measure of cytotoxicity (Tseng, et al., 2015) was affected by NDs (**Fig. S1 a,b,c**). The spheroids exposed to NDs contracted considerably less than untreated spheroids. The surface area of spheroids exposed to 50 and 100 μg mL^{-1} of NDs was 49 and 54% larger than the surface area of untreated spheroids (**Fig. S1d**). Therefore, the results confirmed that NDs reduce the ability of cells to migrate that could be associated to the arrest of cell proliferation, drop in cell viability or disturbance of cytoskeletal organization (Tseng, et al., 2015) – cytotoxicity.

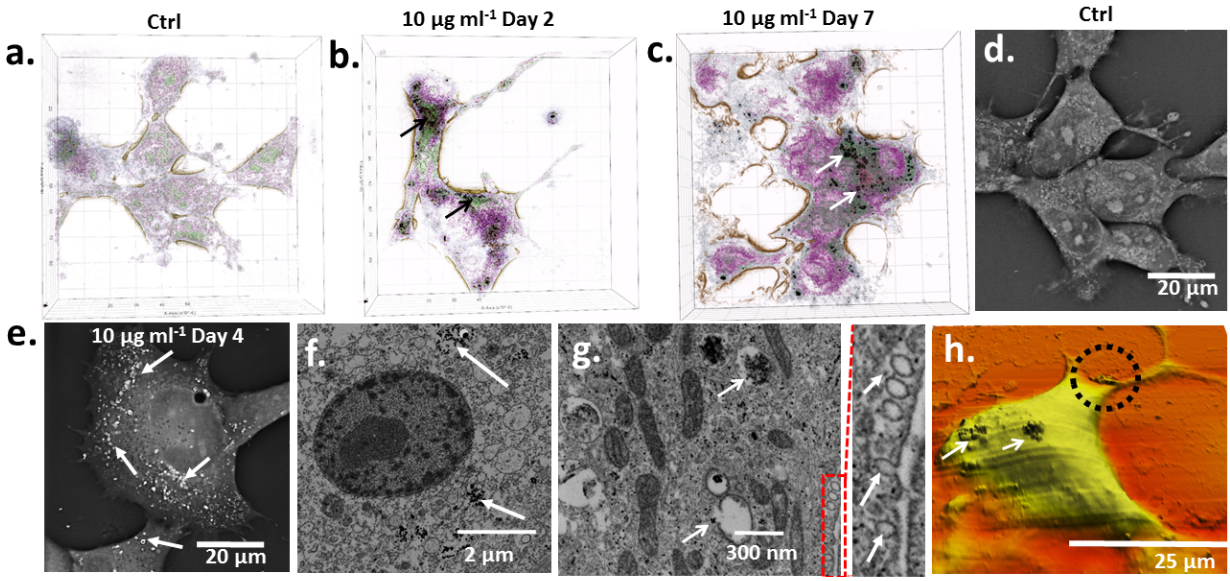

Fig.5: The assessment of nanodiamond (ND) uptake. Holotomography images of (a) control cell, (b) cells exposed to ND at day 2, black arrows indicate the region of ND localization, (c) cells exposed to ND at day 7, white arrows indicate the ND localization, (d) phase contrast image of control cells and (e) cells exposed to ND at day 4; internalized ND (white arrows). (f – g) Scanning electron micrographs of ND treated cell sections (ND white arrows). (h) High resolution 3D image of cell treated with ND.

Analysis of the ND uptake in 3D

3D holotomography, dark field hyperspectral imaging and SEM showed that NDs were readily internalized by cells and were distributed within entire cell structure. 3D images of cells treated with NDs for 2, 4 and 7 days showed the presence of substantial amount of NDs within cells (**Fig. 5 a, b, c, d & e & Fig. S2 a & b**; black stain; black and white arrows). The amount of ND within cells dropped with the time of exposure. Hyperspectral imaging confirmed the same trend (**Fig. S3**). At days 2 and 4, a substantial amount of NDs were found to persist within cell structure (**Fig. S3b**, white arrows). At day 7, the amount of intracellular NDs was reduced (**Fig. S3d**, white arrows).

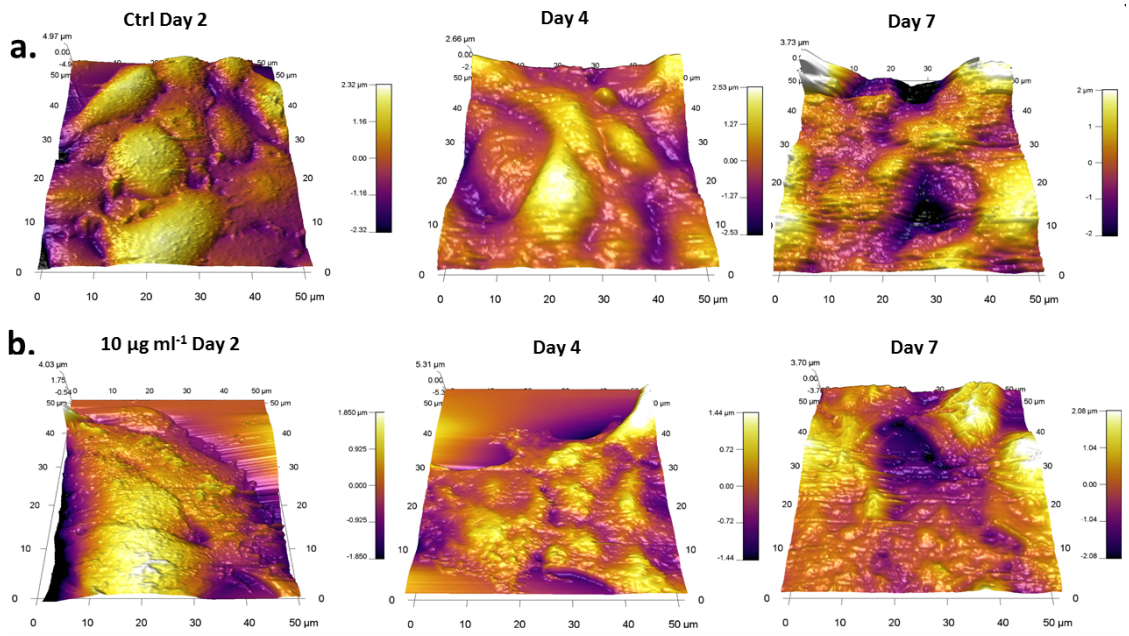

Fig.6: The effect of nanodiamonds (NDs) on the morphology of Fao cell. (a) High resolution atomic force microscopic image of control cells from day 2 to 7 (left to right). (b) AFM images of the cells exposed to ND.

The overall drop of the amount of NDs within individual cells at day 7 could be due to exocytosis or repartition of NDs between cells or during cell division.

Spectral profiles (**Fig. S3e**) collected from control and ND treated cells confirmed that 'bright' features on the cell surface as well as inside the cells were NDs (**Fig. S3, f to h**, white arrows). The uptake of NDs was further confirmed by SEM imaging (**Fig. 5f & g**).

While a small amount of internalized NDs were seen within the endosomal vesicles, a large proportion of NDs escaped the endosomes (breakage of the endosomal sac, white arrows) and were found within the cytoplasm **(Fig. 5g)**. The uptake of NDs into the cells induced the formation of lipid droplets (**Fig. 5f**, red arrows) in the cytoplasm of the cells, which corresponds with stress or injury (Sarhan and Hussein, 2014) and was in agreement with ROS production results.

SEM and AFM images of the cells treated with NDs indicated that the uptake of NDs occurred by a combination of endocytic pathways (formation of endocytic vesicles on the cell membrane **Fig. 5g**, red dotted box and white arrows) and filopodia mediated micropinocytosis (**Fig. 5h**, black circle). These pathways were previously reported to be primary pathways for the uptake of other classes of NDs (Solarska, et al., 2012).

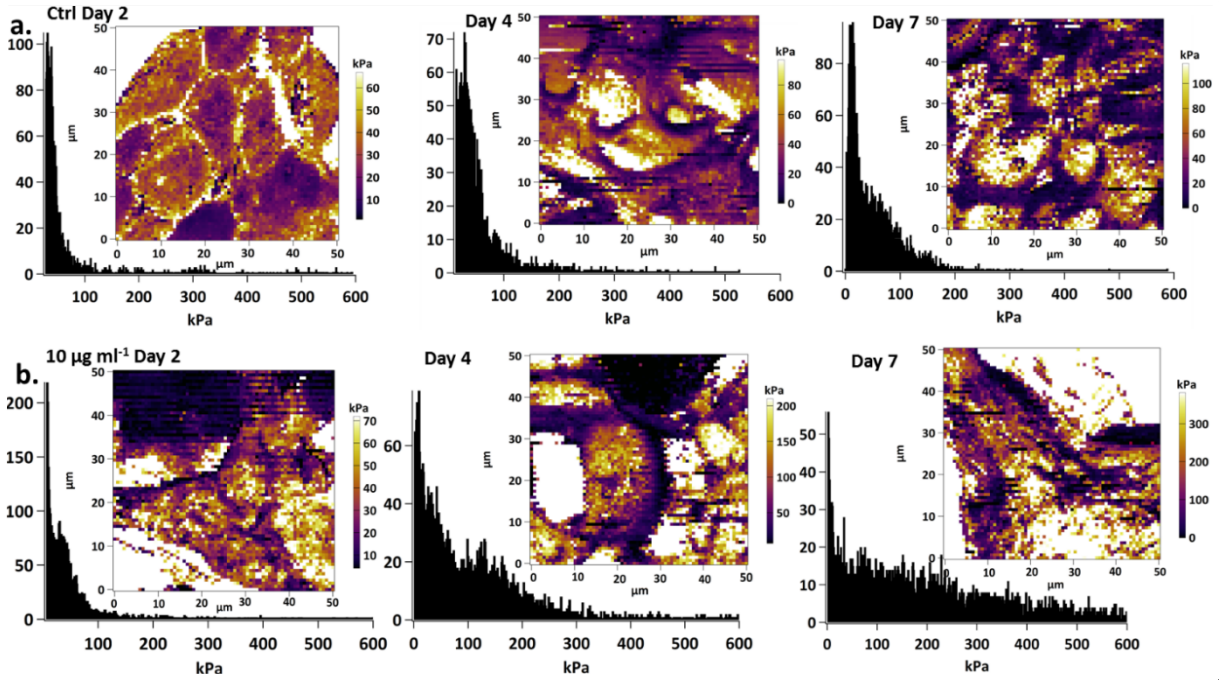

Fig.7: Distribution of stiffness; apparent Young's modulus maps of Fao cells before and after exposure to nanodiamonds (NDs): (a) maps for control cell demonstrates regions of high and low stiffness; no significant changes in stiffness were observed at day 2 and 7; (b) maps for cell exposed to 10 µg·mL^{-1} of NDs confirmed increased stiffness that was correlated to the duration of the exposure.

duration of exposure; the longer the exposure to NDs, the higher the stiffness was.

At day 7, the median stiffness of control cells remained 24 kPa, while for cells treated with

NDs, it increased depending on ND concentration to 76 kPa for 10 μg·mL^{-1} and 298 kPa for 50 μg·mL^{-1}.

Detailed analysis of stiffness using log normal regression (**Fig. 8 a, b**; **Fig. S4 a, b**) confirmed that NDs led to increase in cell stiffness that was dependent on the duration of the exposure. Similarly, box whisker plots confirmed that cell stiffness increased with the exposure time to NDs and the increase was not dose dependent (**Fig. 8 a**,**b**). Interestingly, we found that short term exposure to high concentration (50 μg·mL^{-1}) of NDs led to significant increase in cell stiffness at day 2 (**Fig. 8 b**), highlighting the negative effect of NDs at relatively high concentration.

Furthermore, we calculated the geometric standard deviation (GSD) of the stiffness distribution using 16th and 84th percentile values from the cumulative data. GSD increased from ~1.5 for untreated cells to ~3.52 for ND-treated cells (10 μg·mL^{-1}).

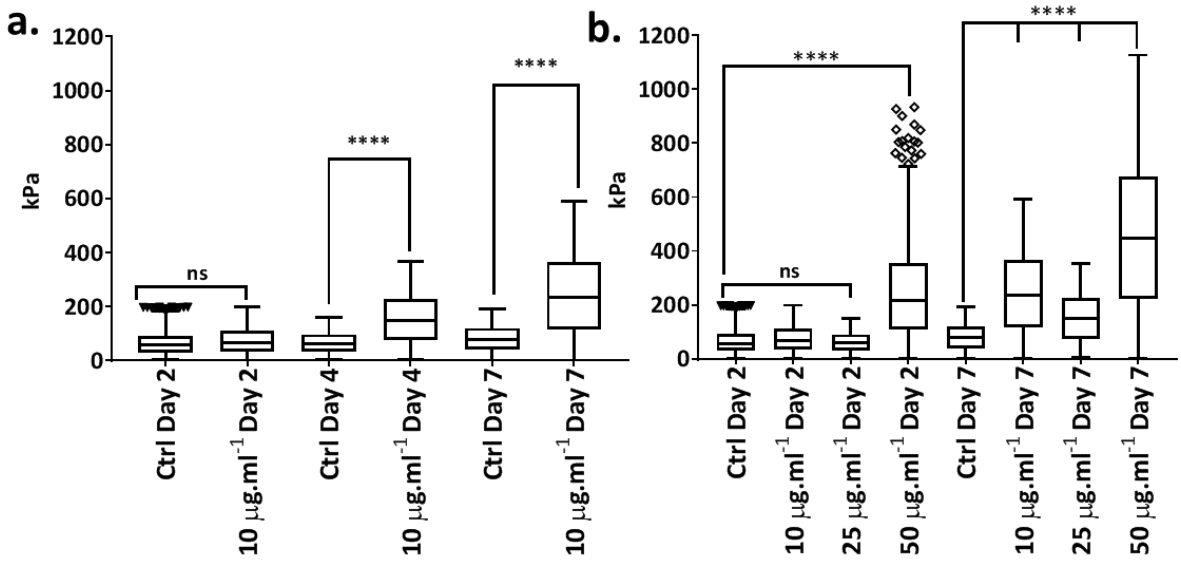

Fig. 8: Box and whiskers plot for apparent Young's modulus distribution. (a) Comparison of cell stiffness of control cell and cells exposed to 10 μg·mL^{-1} ND from day 2 to 7. Stiffness of cell exposed to NDs showed significant increase in cell stiffness in comparison to control cells from day 4 onwards. (b) Comparison of cell stiffness between the control cells and cells exposed to 10, 25 and 50 μg·mL^{-1} ND at day 2 and 7. (One-way ANOVA, Tukey's multiple comparison).

Discussion

Constraints in the tools and assays commonly used for measuring effects of nanoparticles on cell function, limit the accuracy of nanotoxicity assessment. An exponentially growing number of reports on toxicity of nanoparticles (Bettini, et al., 2017, Peng, et al., 2019, Setyawati, et al., 2013, Setyawati, et al., 2017, Yamashita, et al., 2011, Pinget, et al., 2019 and the recalls of common nanoparticles used for medical imaging (Wei, et al., 2017) confirms that more accurate nanotoxicity testing approaches are needed.

Despite contradicting safety records, NDs are being currently re-explored for magnetic resonance imaging. Our previous study confirmed that NDs can lead to denaturation and conformational changes of intra- and extracellular proteins and lead to the formation of fibrillary amyloid-like proteins (Khanal, et al., 2016). It is therefore necessary to determine safety of NDs using high-resolution methods before NDs progress to clinical trials.

The primary objective of this work was to demonstrate difference in NDs toxicity depending on cell culture model, 2D *vs*. 3D (mini-livers), by applying label-free, high-resolution and high-throughput approach.

NDs induce ROS-mediated, concentration- and time-dependent cytotoxicity in liver cells

Our results showed that the exposure of cells to NDs for 48 h at the concentrations of 25 $\mu g \cdot mL^{-1}$ and above led to substantial drop in Fao cell viability in 2D cell culture model. The drop could be associated with an inability of cells to excrete NDs. We confirmed that NDs were internalized within 24 h (**Fig. 5b**) and persisted within cell cytosol (**Fig. 5f and g**). NDs were able to rupture the endosomal membrane and spread inside the cell cytosol, where they may potentially induce protein damage (Khanal, et al., 2016). The lack of measurable cytotoxicity in the first 24 h could also be related to sedimentation time of NDs and

progressively increasing number of NDs that reached cells (Cohen, et al., 2013). Therefore, short-term experiments which are conducted for 24 h or less may not be conclusive and effective in testing NDs cytotoxicity (Khanal, et al., 2017, Yu, et al., 2005, Liu, et al., 2007, Schrand, et al., 2007). One solution could be measurements of intracellular concentrations of NDs that may provide additional insights into the toxicity of NDs.

Next, we confirmed the effects of NDs on cell function using long-term studies and real-time impedance measurements. Since impedance measurements provide a direct measure of cell growth and membrane integrity, the drop in impedance is associated with the damage to the cell membrane, cell detachment (loss of biological function) and the inhibition of cell proliferation (Peper, et al., 2014). Indeed, we observed a substantial drop in impedance after 90 h of ND exposure at the concentration as low as 10 $\mu g \cdot mL^{-1}$ (**Fig. 3a**), which indicated that NDs induced cytotoxicity. The decrease in cell membrane integrity was further confirmed by the evaluating the cytoskeletal structure (f-actin) (**Fig. 3e**) and the assessment of cell morphology in 3D (**Fig. 5b**). Image of cell cytoskeleton and 3D morphology of cells confirmed that the organization of cytoskeleton (f-actin) was negatively affected by NDs and led to the formation of giant cells. The formation of giant cells after exposure to NDs may be due to the disorganization of cytoskeleton (f-actin) leading to arrest of cells division and proliferation (Holt, et al., 2010).

Notably, NDs induced the overproduction of ROS (**Fig. 3c**). Since, intracellular ROS leads to the generation of protein radicals, lipid peroxidation and alteration of gene expression, we concluded that NDs impaired cellular function and led to cell death and to the loss of membrane integrity. Similar effects have been observed for human endothelial cell exposed to detonation NDs (Solarska, et al., 2012, Setyawati, et al., 2016).

Semi-high throughput label-free real-time assay accelerates toxicity assessment

Our results demonstrated that mini-liver models (ring closure and dot assays) that represent 3D multicellular environment, allow for faster and effective assessment of cytotoxicity. The ring closure and dot assays are wound healing and migration assays conducted in 3D. Similar assays conducted in 2D (aka scratch assays), where the cells migrate to close a mechanically or electrically induced hole or a linear scratch are widely used to assess toxicity associated with drugs and chemicals (Timm, et al., 2013, Tseng, et al., 2015). Both dot (**Fig. S1**) and ring closure assays (**Fig. 4**) confirmed that NDs reduced the ability of cells to migrate as indicated by slower rate of ring closure and dot shrinkage. This could also be due to the arrest of cell proliferation after exposure to NDs. This result was not in full agreement with the 2D viability assays where substantial differences in the cytotoxicity of NDs was not demonstrated until 48 h of exposure. However, both the ring closure and dot assays were able to detect the effects of NDs within 48 h of exposure. These results suggest mini-liver models mimic the extracellular environment more precisely and are more sensitive for testing nanotoxicity. While we could expect lower toxicity when using 3D models, our study showed opposite, which is likely to be due to direct cell-cell contact and shorter path for intracellular communication as it is observed in physiological conditions. The lower cytotoxicity observed in 2D cell culture models could be due to more rapid proliferation of cells in 2D environment compared to the cells cultured in 3D (Edmondson, et al., 2014). Another consideration could be that nanoparticles are known to induce oxidation of tetrazolium salt (WST-8) which may overestimate the viability of cells in the 2D culture models specifically.

Since mini-liver models were magnetically bioprinted using cells pretreated with magnetic nanoparticles, it was essential to establish control experiments using magnetic

nanoparticle only. Control experiments allowed us to decouple the influence of magnetic nanoparticles from the influence of nanodiamond on final results. Theoretically, all types of nanoparticles have an impact on cell function and there is a likelihood that magnetic nanoparticles might have interfered with the measurements conducted here. However, to reduce the risk of interference we used commercially available nanoparticles that were previously demonstrated to have no or minimal impact on cell function (Timm, et al., 2013, Tseng, et al., 2015). Additionally, in the result interpretation we compared the results for nanodiamond treated samples to control experiments to avoid any bias potentially introduced by magnetic nanoparticles. It is also well-established that impact of nanoparticles on cells is concentration-dependent. Therefore, in our study we used minimum concentration of magnetic nanoparticles (8 $\mu L/cm^2$) and the magnetic force (30-500 G) to allow effective bioprinting of the models. These conditions for magnetic bioprinting were previously validated and shown to have insignificant effect on cell proliferation, metabolism or inflammatory response in multiple cell culture models (Timm, et al., 2013, Tseng, et al., 2015). Nevertheless, similarly to fluorescent probes, potential additive effects of magnetic nanoparticles and nanodiamond on cells cannot be completely excluded, therefore we conducted a wide range of assays in both 2 and 3D configuration to validate the results and ensure their robustness.

Mechanobiological properties of cell as a biomarker for toxicity assessment

Mechanical properties are key markers of cell function, motility, proliferation, rigidity (stiffness), contractility, tissue organization and many other vital biological processes (Cai, et al., 2010, Haghi, et al., 2015, Berntsen, et al., 2010). Our results confirmed that NDs induced increased stiffness of cells depending on the concentration of NDs and the duration of exposure. When NDs are internalized by cells and retained in the cytoplasm,

there is a possibility of ND particles interacting with cytoskeleton and biomolecules that are present within cell cytoplasm. This interaction could lead to cytoskeletal disruption and increase in cell stiffness (**Fig. 7**). The increase in cell stiffness after the exposure to NDs could also be associated with the increased production of ROS (Dong, et al., 2013, Subbiah, et al., 2013, Buyukhatipoglu and Clyne, 2011). In general, nanoparticles that are internalized by cells may interact with the key proteins responsible for cytoskeleton organization. Cytoskeleton reorganization is often controlled by small GTP-binding proteins such as Ras, Rho and Rac proteins. Ras proteins regulates membrane ruffling, pinocytosis and formation of stress fibers. Rac is involved only in the formation of ruffles, whereas Rho regulates the formation of stress fibers (Gupta and Curtis, 2004). Hence, if these proteins interact with nanoparticles, they may undergo conformational changes. Subsequently, changes to the protein conformation (i.e. denaturation) will dysregulate fundamental signaling pathways for cytoskeletal organization and are likely to compromise cell function or even cause cell death (Khanal, et al., 2016).

To reduce the uncertainty and variations in stiffness measurements between the samples, all the cells were fixed at a similar point of cell cycle following the established protocol (Haghi, et al., 2015, Jaffar, et al., 2018). All cells had to be fixed to conduct the high-resolution mechanical mapping on cells which usually takes 4 to 5 hours. Since, living cells are motile they may move during the experiment, which is further stimulated by indentations. This makes it nearly impossible to conduct high resolution mapping especially during cell migration, because the cytoskeleton of the cells contracts and thus significantly impacts cell stiffness. As a result, only high speed or low resolution mapping can be conducted on live cells. High speed imaging distorts the stiffness values due to the friction between the tip and the cell and the dynamic, viscoelastic reaction of the cell

membrane. Previous studies have also confirmed that fixation of cells allow to obtain reproducible results for the apparent Young's modulus of cells (Jaffar, et al., 2018).

Our results demonstrated that mechanobiological properties of cells can be used as a biomarker in evaluating impact of nanoparticles on cell function.

Conclusion

In this study, we demonstrated that ND particles induced ROS mediated cytotoxicity (Fao cells), which was both concentration and exposure-time dependent. Specifically, NDs reduced cell viability and impaired cell membrane integrity. Furthermore, NDs decreased the ability of cells to migrate and substantially increased cell stiffness. Cumulatively, these results confirmed that NDs adversely impact overall cell function at concentrations above 25 $\mu g \cdot mL^{-1}$.

Interestingly, our results showed that mini-livers were able to detect the cytotoxicity of NDs within 48 h while 2D cell culture models did not reveal substantial differences in cell growth and viability between control and treated samples in the first 48 h.

In conclusion, to test nanotoxicity, we applied a new approach that utilized label-free and high-resolution methods including impedance spectroscopy, molecular force probe, 3D holotomography, dark field hyperspectral imaging and semi-high throughput ring and dot assays. We demonstrated that this approach offers ultra-high sensitivity and allows for rapid and effective nanotoxicity assessment. These capabilities complement traditional experimental approaches.

Author details

[1] The University of Sydney, Sydney Nano Institute, Faculty of Medicine and Health, Sydney Pharmacy School, NSW 2006, Australia

[2]Brigham & Women's Hospital, Harvard Medical School, Boston, USA

[3]School of Computer Science and Engineering, University of New South Wales, NSW 2052, Australia

[4]School of Materials Science and Engineering, Nanyang Technological University, Singapore

[5]Department of Biomedical Sciences, College of Life and Health Sciences, Chubu University, Aichi Prefecture 487-8501, Japan

[6]CytoViva, Inc.570 Devall Drive, Suite 301, Auburn, AL 36832, USA

[7]School of Physics, The University of Sydney, NSW 2006, Australia

[8]Division of Biomaterials and Tissue Engineering, UCL Eastman Dental Institute, University College London, 256 Gray's Inn Road, London WC1X 8LD, UK

[9]The Discoveries Centre for Regenerative and Precision Medicine, UCL Campus, London, UK

[10]Department of Nanobiomedical Science & BK21 Plus NBM Global Research Center for Regenerative Medicine, Dankook University, Cheonan, Korea

[11]School of Information Technologies, Faculty of Engineering and Information Technologies, The University of Sydney, NSW 2006, Australia

Conflict of Interest

The authors declare no competing financial interest.

Author Contributions

W.Ch. initiated, co-designed, supervised the project and wrote the manuscript; D.K. co-designed, carried out the core of experiments and wrote the manuscript; S.Y. conducted and analysed XPS experiments; G.G. and J.C.K. conducted and analysed XRD experiments;

A.K. conducted and analysed FTIR experiments; F.Z., Y.S., W.C. developed the software for the analysis of ring closure and spheroid shrinkage assay; S.M. and J.U. conducted the experiments with hyperspectral imaging; A.G conducted nanoparticle tracking analysis and TEM measurements; H.H. analysed results of 3D assays; I.R. and K.W.Ng provided intellectual input into experimental design and analyses of nanotoxicity and hepatotoxicity. All authors reviewed the manuscript and provided intellectual inputs.

Data Availability

The raw/processed data required to reproduce these findings can be shared as upon request.

References

S. Bettini, E. Boutet-Robinet, C. Cartier, C. Coméra, E. Gaultier, J. Dupuy, N. Naud, S. Taché, P. Grysan and S. Reguer. 2017. Food-grade TiO 2 impairs intestinal and systemic immune homeostasis, initiates preneoplastic lesions and promotes aberrant crypt development in the rat colon. Scientific Reports 7:40373.

F. Peng, M. I. Setyawati, J. K. Tee, X. Ding, J. Wang, M. E. Nga, H. K. Ho and D. T. Leong. 2019. Nanoparticles promote in vivo breast cancer cell intravasation and extravasation by inducing endothelial leakiness. Nature nanotechnology 14:279.

M. Setyawati, C. Y. Tay, S. Chia, S. Goh, W. Fang, M. Neo, H. C. Chong, S. Tan, S. C. J. Loo and K. Ng. 2013. Titanium dioxide nanomaterials cause endothelial cell leakiness by disrupting the homophilic interaction of VE–cadherin. Nature communications 4:1673.

M. I. Setyawati, C. Y. Tay, B. H. Bay and D. T. Leong. 2017. Gold nanoparticles induced endothelial leakiness depends on particle size and endothelial cell origin. ACS nano 11:5020-5030.

K. Yamashita, Y. Yoshioka, K. Higashisaka, K. Mimura, Y. Morishita, M. Nozaki, T. Yoshida, T. Ogura, H. Nabeshi and K. Nagano. 2011. Silica and titanium dioxide nanoparticles cause pregnancy complications in mice. Nature nanotechnology 6:321.

G. Pinget, J. Tan, B. Janac, N. O. Kaakoush, A. S. Angelatos, J. O'Sullivan, Y. C. Koay, F. Sierro, J. Davis, S. K. Divakarla, D. Khanal, R. J. Moore, D. Stanley, W. Chrzanowski and L. Macia. 2019. Impact of the Food Additive Titanium Dioxide (E171) on Gut Microbiota-Host Interaction. Frontiers in Nutrition 6.

A. Alhaddad, M. P. Adam, J. Botsoa, G. Dantelle, S. Perruchas, T. Gacoin, C. Mansuy, S. Lavielle, C. Malvy and F. Treussart. 2011. Nanodiamond as a vector for siRNA delivery to Ewing sarcoma cells. Small 7:3087-3095.

J. Li, Y. Zhu, W. Li, X. Zhang, Y. Peng and Q. Huang. 2010. Nanodiamonds as intracellular transporters of chemotherapeutic drug. Biomaterials 31:8410-8418.

D. Wang, Y. Tong, Y. Li, Z. Tian, R. Cao and B. Yang. 2013. PEGylated nanodiamond for chemotherapeutic drug delivery. Diamond and Related Materials 36:26-34.
L. Zhao, Y.-H. Xu, T. Akasaka, S. Abe, N. Komatsu, F. Watari and X. Chen. 2014. Polyglycerol-coated nanodiamond as a macrophage-evading platform for selective drug delivery in cancer cells. Biomaterials 35:5393-5406.
Q. Zhang, V. N. Mochalin, I. Neitzel, K. Hazeli, J. Niu, A. Kontsos, J. G. Zhou, P. I. Lelkes and Y. Gogotsi. 2012. Mechanical properties and biomineralization of multifunctional nanodiamond-PLLA composites for bone tissue engineering. Biomaterials 33:5067-5075.
X. Luo, H. Zhang, Z. Cao, N. Cai, Y. Xue and F. Yu. 2016. A simple route to develop transparent doxorubicin-loaded nanodiamonds/cellulose nanocomposite membranes as potential wound dressings. Carbohydrate Polymers 143:231-238.
M. A. Brady, A. Renzing, T. E. Douglas, Q. Liu, S. Wille, M. Parizek, L. Bacakova, A. Kromka, M. Jarosova and G. Godier. 2015. Development of composite poly (lactide-co-glycolide)-nanodiamond scaffolds for bone cell growth. Journal of nanoscience and nanotechnology 15:1060-1069.
L. M. Manus, D. J. Mastarone, E. A. Waters, X.-Q. Zhang, E. A. Schultz-Sikma, K. W. MacRenaris, D. Ho and T. J. Meade. 2009. Gd (III)-nanodiamond conjugates for MRI contrast enhancement. Nano letters 10:484-489.
J.-I. Chao, E. Perevedentseva, P.-H. Chung, K.-K. Liu, C.-Y. Cheng, C.-C. Chang and C.-L. Cheng. 2007. Nanometer-sized diamond particle as a probe for biolabeling. Biophysical journal 93:2199-2208.
D.-K. Lee, T. Kee, Z. Liang, D. Hsiou, D. Miya, B. Wu, E. Osawa, E. K.-H. Chow, E. C. Sung and M. K. Kang. 2017. Clinical validation of a nanodiamond-embedded thermoplastic biomaterial. Proceedings of the National Academy of Sciences:201711924.
J.-P. Boudou, P. A. Curmi, F. Jelezko, J. Wrachtrup, P. Aubert, M. Sennour, G. Balasubramanian, R. Reuter, A. Thorel and E. Gaffet. 2009. High yield fabrication of fluorescent nanodiamonds. Nanotechnology 20:235602-235602.
M. V. Baidakova, Y. A. Kukushkina, A. A. Sitnikova, M. A. Yagovkina, D. A. Kirilenko, V. V. Sokolov, M. S. Shestakov, A. Y. Vul', B. Zousman and O. Levinson. 2013. Structure of nanodiamonds prepared by laser synthesis. Physics of the Solid State 55:1747-1753.
H. Moche, V. Paget, D. Chevalier, E. Lorge, N. Claude, H. A. Girard, J. C. Arnault, S. Chevillard and F. Nesslany. 2017. Carboxylated nanodiamonds can be used as negative reference in in vitro nanogenotoxicity studies. Journal of Applied Toxicology 37:954-961.
V. Paget, J. A. Sergent, R. Grall, S. Altmeyer-Morel, H. A. Girard, T. Petit, C. Gesset, M. Mermoux, P. Bergonzo, J. C. Arnault and S. Chevillard. 2014. Carboxylated nanodiamonds are neither cytotoxic nor genotoxic on liver, kidney, intestine and lung human cell lines. Nanotoxicology 8 Suppl 1:46-56.
A. Krüger. 2006. Hard and soft: biofunctionalized diamond. Angewandte Chemie International Edition 45:6426-6427.
J. Mytych, A. Lewinska, A. Bielak-Zmijewska, W. Grabowska, J. Zebrowski and M. Wnuk. 2014. Nanodiamond-mediated impairment of nucleolar activity is accompanied by oxidative stress and DNMT2 upregulation in human cervical carcinoma cells. Chemico-biological interactions 220:51-63.
Y. Yuan, Y. Chen, J.-H. Liu, H. Wang and Y. Liu. 2009. Biodistribution and fate of nanodiamonds< i> in vivo</i>. Diamond and related materials 18:95-100.

Z. Chu, K. Miu, P. Lung, S. Zhang, S. Zhao, H.-C. Chang, G. Lin and Q. Li. 2015. Rapid endosomal escape of prickly nanodiamonds: implications for gene delivery. Scientific reports 5:11661.
J. Lee, G. D. Lilly, R. C. Doty, P. Podsiadlo and N. A. Kotov. 2009. In vitro toxicity testing of nanoparticles in 3D cell culture. Small 5:1213-1221.
S. L. Chia, C. Y. Tay, M. I. Setyawati and D. T. Leong. 2015. Biomimicry 3D gastrointestinal spheroid platform for the assessment of toxicity and inflammatory effects of zinc oxide nanoparticles. Small 11:702-712.
K. M. Yamada and E. Cukierman. 2007. Modeling tissue morphogenesis and cancer in 3D. Cell 130:601-610.
A. C. Daquinag, G. R. Souza and M. G. Kolonin. 2012. Adipose tissue engineering in three-dimensional levitation tissue culture system based on magnetic nanoparticles. Tissue Engineering Part C: Methods 19:336-344.
A. R. Collins, B. Annangi, L. Rubio, R. Marcos, M. Dorn, C. Merker, I. Estrela-Lopis, M. R. Cimpan, M. Ibrahim, E. Cimpan, M. Ostermann, A. Sauter, N. E. Yamani, S. Shaposhnikov, S. Chevillard, V. Paget, R. Grall, J. Delic, F. G.-. de-Cerio, B. Suarez-Merino, V. Fessard, K. N. Hogeveen, L. M. Fjellsbø, E. R. Pran, T. Brzicova, J. Topinka, M. J. Silva, P. E. Leite, A. R. Ribeiro, J. M. Granjeiro, R. Grafström, A. Prina-Mello and M. Dusinska. 2017. High throughput toxicity screening and intracellular detection of nanomaterials. Wiley Interdisciplinary Reviews: Nanomedicine and Nanobiotechnology 9:e1413.
X. Cai, X. Xing, J. Cai, Q. Chen, S. Wu and F. Huang. 2010. Connection between biomechanics and cytoskeleton structure of lymphocyte and Jurkat cells: An AFM study. Micron 41:257-262.
M. Haghi, D. Traini, L. G. Wood, B. Oliver, P. M. Young and W. Chrzanowski. 2015. A 'soft spot'for drug transport: modulation of cell stiffness using fatty acids and its impact on drug transport in lung model. Journal of Materials Chemistry B 3:2583-2589.
B. P. Head, H. H. Patel and P. A. Insel. 2014. Interaction of membrane/lipid rafts with the cytoskeleton: impact on signaling and function: membrane/lipid rafts, mediators of cytoskeletal arrangement and cell signaling. Biochimica et Biophysica Acta (BBA)-Biomembranes 1838:532-545.
S. E. Cross, Y.-S. Jin, J. Rao and J. K. Gimzewski. 2007. Nanomechanical analysis of cells from cancer patients. Nature Nanotechnology 2:780.
M. Li, L. Liu, N. Xi, Y. Wang, Z. Dong, X. Xiao and W. Zhang. 2012. Atomic force microscopy imaging and mechanical properties measurement of red blood cells and aggressive cancer cells. Science China Life Sciences 55:968-973.
D. Kirmizis and S. Logothetidis. 2010. Atomic force microscopy probing in the measurement of cell mechanics. International journal of nanomedicine 5:137.
H.-J. Butt, B. Cappella and M. Kappl. 2005. Force measurements with the atomic force microscope: Technique, interpretation and applications. Surface science reports 59:1-152.
H. K. Webb, V. K. Truong, J. Hasan, R. J. Crawford and E. P. Ivanova. 2011. Physico-mechanical characterisation of cells using atomic force microscopy—current research and methodologies. Journal of microbiological methods 86:131-139.
K. J. Ong, T. J. MacCormack, R. J. Clark, J. D. Ede, V. A. Ortega, L. C. Felix, M. K. Dang, G. Ma, H. Fenniri, J. G. Veinot and G. G. Goss. 2014. Widespread nanoparticle-assay interference: implications for nanotoxicity testing. PloS one 9:e90650.

D. Chaya, C. Fougère-Deschatrette and M. C. Weiss. 1997. Liver-enriched transcription factors uncoupled from expression of hepatic functions in hepatoma cell lines. Molecular and cellular biology 17:6311-6320.
D. Cassio and M. C. Weiss. 1979. Expression of fetal and neonatal hepatic functions by mouse hepatoma-rat hepatoma hybrids. Somatic Cell and Molecular Genetics 5:719-738.
J. Deschatrette, C. Fougere-Deschatrette, L. Corcos and R. T. Schimke. 1985. Expression of the mouse serum albumin gene introduced into differentiated and dedifferentiated rat hepatoma cells. Proceedings of the National Academy of Sciences 82:765-769.
D. Khanal, H. Hau, A. Kondyurin, D. Fu, I. Ramzan and W. Chrzanowski. 2017. Nanotoxicity of nanodiamond in two and three dimensional liver models. International Journal of Nanotechnology 14:133-154.
H. Hau, D. Khanal, L. Rogers, N. Suchowerska, R. Kumar, S. Sridhar, D. McKenzie and W. Chrzanowski. 2016. Dose enhancement and cytotoxicity of gold nanoparticles in colon cancer cells when irradiated with kilo- and mega-voltage radiation. Bioengineering & translational medicine 1:94-102.
D. M. Timm, J. Chen, D. Sing, J. A. Gage, W. L. Haisler, S. K. Neeley, R. M. Raphael, M. Dehghani, K. P. Rosenblatt and T. Killian. 2013. A high-throughput three-dimensional cell migration assay for toxicity screening with mobile device-based macroscopic image analysis. Scientific reports 3:1-8.
H. Tseng, J. A. Gage, T. Shen, W. L. Haisler, S. K. Neeley, S. Shiao, J. Chen, P. K. Desai, A. Liao and C. Hebel. 2015. A spheroid toxicity assay using magnetic 3D bioprinting and real-time mobile device-based imaging. Scientific reports 5:13987.
V. N. Mochalin, O. Shenderova, D. Ho and Y. Gogotsi. 2012. The properties and applications of nanodiamonds. Nature Nanotechnology 7:11-23.
D. Khanal, A. Kondyurin, H. Hau, J. C. Knowles, O. Levinson, I. Ramzan, D. Fu, C. Marcott and W. Chrzanowski. 2016. Biospectroscopy of Nanodiamond-Induced Alterations in Conformation of Intra- and Extracellular Proteins: A Nanoscale IR Study. Analytical Chemistry 88:7530-7538.
F. Y. Xie, W. G. Xie, L. Gong, W. H. Zhang, S. H. Chen, Q. Z. Zhang and J. Chen. 2010. Surface characterization on graphitization of nanodiamond powder annealed in nitrogen ambient. Surface and Interface Analysis 42:1514-1518.
O. M. M. Sarhan and R. M. Hussein. 2014. Effects of intraperitoneally injected silver nanoparticles on histological structures and blood parameters in the albino rat. International journal of nanomedicine 9:1505.
K. Solarska, A. Gajewska, W. Kaczorowski, G. Bartosz and K. Mitura. 2012. Effect of nanodiamond powders on the viability and production of reactive oxygen and nitrogen species by human endothelial cells. Diamond and Related Materials 21:107-113.
H. Wei, O. T. Bruns, M. G. Kaul, E. C. Hansen, M. Barch, A. Wiśniowska, O. Chen, Y. Chen, N. Li, S. Okada, J. M. Cordero, M. Heine, C. T. Farrar, D. M. Montana, G. Adam, H. Ittrich, A. Jasanoff, P. Nielsen and M. G. Bawendi. 2017. Exceedingly small iron oxide nanoparticles as positive MRI contrast agents. Proceedings of the National Academy of Sciences of the United States of America 114:2325-2330.
J. Cohen, G. Deloid, G. Pyrgiotakis and P. Demokritou. 2013. Interactions of engineered nanomaterials in physiological media and implications for in vitro dosimetry. Nanotoxicology 7:417-431.

S.-J. Yu, M.-W. Kang, H.-C. Chang, K.-M. Chen and Y.-C. Yu. 2005. Bright Fluorescent Nanodiamonds: No Photobleaching and Low Cytotoxicity. Journal of the American Chemical Society 127:17604-17605.
K.-K. Liu, C.-L. Cheng, C.-C. Chang and J.-I. Chao. 2007. Biocompatible and detectable carboxylated nanodiamond on human cell. Nanotechnology 18:325102.
A. M. Schrand, L. Dai, J. J. Schlager, S. M. Hussain and E. Osawa. 2007. Differential biocompatibility of carbon nanotubes and nanodiamonds. Diamond and Related Materials 16:2118-2123.
J. K. Peper, H. Schuster, M. W. Löffler, B. Schmid-Horch, H.-G. Rammensee and S. Stevanović. 2014. An impedance-based cytotoxicity assay for real-time and label-free assessment of T-cell-mediated killing of adherent cells. Journal of immunological methods 405:192-198.
B. D. Holt, P. A. Short, A. D. Rape, Y.-l. Wang, M. F. Islam and K. N. Dahl. 2010. Carbon Nanotubes Reorganize Actin Structures in Cells and ex Vivo. ACS Nano 4:4872-4878.
M. I. Setyawati, V. N. Mochalin and D. T. Leong. 2016. Tuning Endothelial Permeability with Functionalized Nanodiamonds. ACS Nano 10:1170-1181.
R. Edmondson, J. J. Broglie, A. F. Adcock and L. Yang. 2014. Three-dimensional cell culture systems and their applications in drug discovery and cell-based biosensors. Assay Drug Dev Technol 12:207-218.
P. Berntsen, C. Park, B. Rothen-Rutishauser, A. Tsuda, T. Sager, R. Molina, T. Donaghey, A. M. Alencar, D. Kasahara and T. Ericsson. 2010. Biomechanical effects of environmental and engineered particles on human airway smooth muscle cells. Journal of the Royal Society Interface:rsif20100068.
C. Dong, M. L. Kashon, D. Lowry, J. S. Dordick, S. H. Reynolds, Y. Rojanasakul, L. M. Sargent and C. Z. Dinu. 2013. Exposure to carbon nanotubes leads to changes in the cellular biomechanics. Advanced healthcare materials 2:945-951.
R. Subbiah, S. Ramasundaram, P. Du, K. Hyojin, D. Sung, K. Park, N.-E. Lee, K. Yun and K. J. Choi. 2013. Evaluation of cytotoxicity, biophysics and biomechanics of cells treated with functionalized hybrid nanomaterials. Journal of The Royal Society Interface 10:20130694.
K. Buyukhatipoglu and A. M. Clyne. 2011. Superparamagnetic iron oxide nanoparticles change endothelial cell morphology and mechanics via reactive oxygen species formation. Journal of Biomedical Materials Research Part A 96:186-195.
A. K. Gupta and A. S. Curtis. 2004. Lactoferrin and ceruloplasmin derivatized superparamagnetic iron oxide nanoparticles for targeting cell surface receptors. Biomaterials 25:3029-3040.
J. Jaffar, S.-H. Yang, S. Y. Kim, H.-W. Kim, A. Faiz, W. Chrzanowski and J. K. Burgess. 2018. Greater cellular stiffness in fibroblasts from patients with idiopathic pulmonary fibrosis. American Journal of Physiology-Lung Cellular and Molecular Physiology 315:L59-L65.

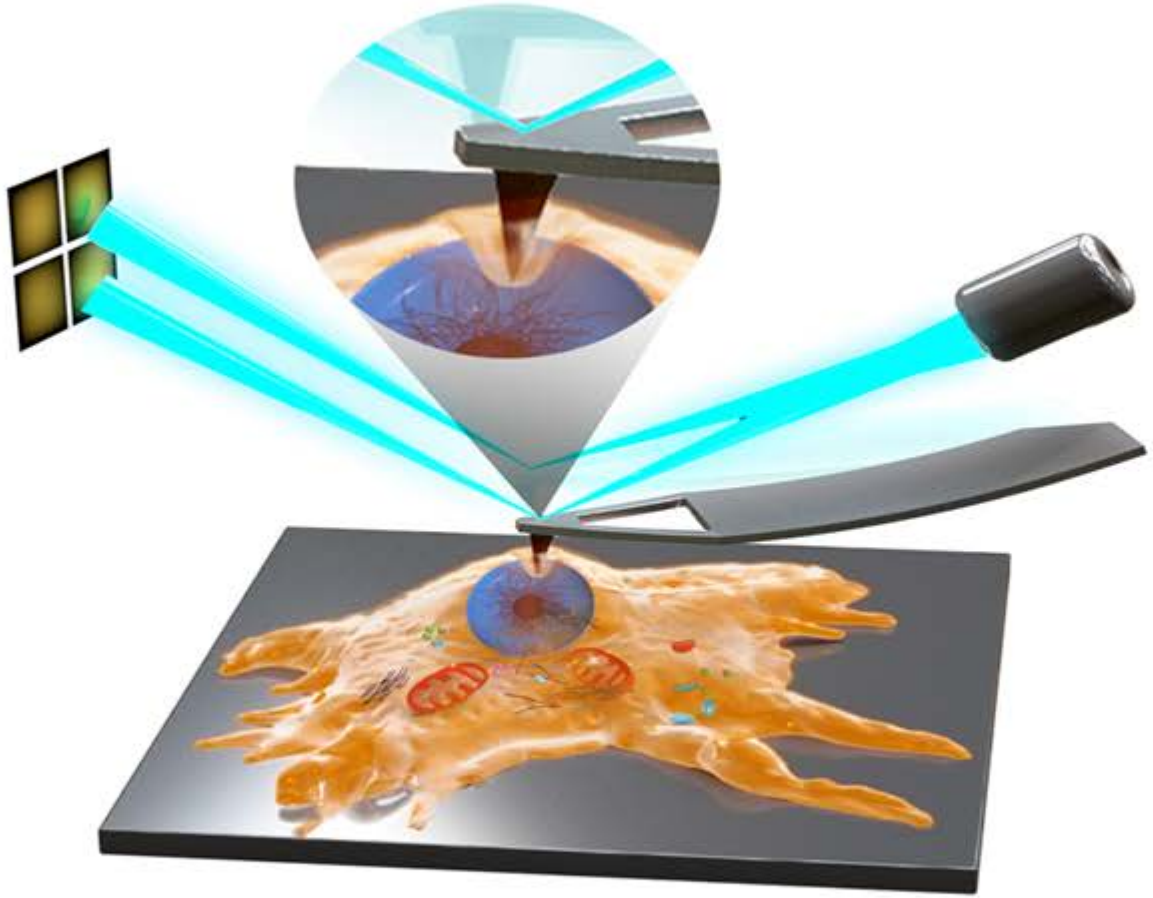

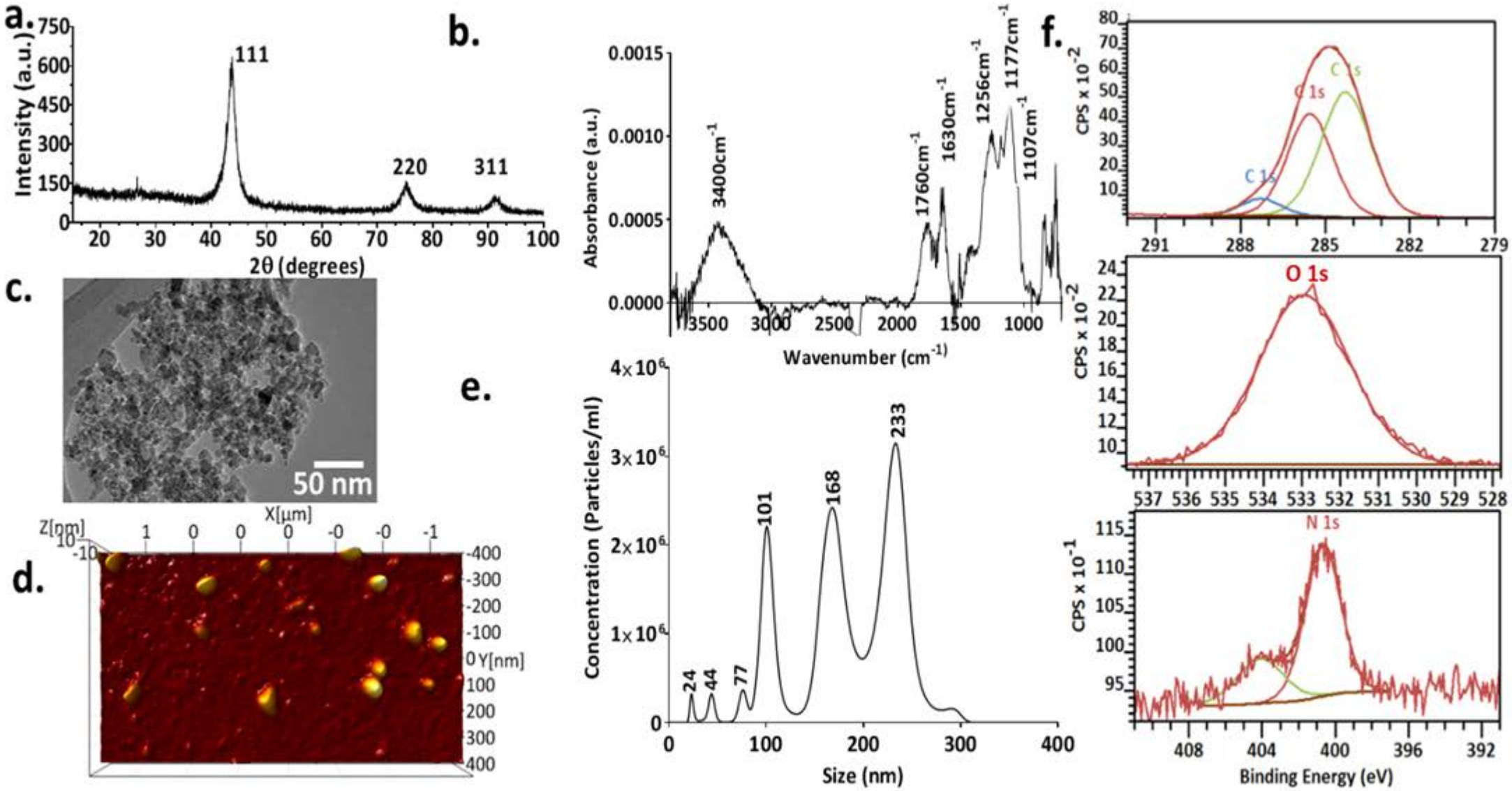
a.
Intensity (a.u.)
2θ (degrees)
111
220
311
b.
Absorbance (a.u.)
Wavenumber (cm-1)
3400cm-1
1760cm-1
1630cm-1
1256cm-1
1177cm-1
1107cm-1
c.
50 nm
d.
X[μm]
Z[nm]
Y[nm]
e.
Concentration (Particles/ml)
Size (nm)
24
44
77
101
168
233
f.
CPS x 10-2
C 1s
O 1s
CPS x 10-1
N 1s
Binding Energy (eV)

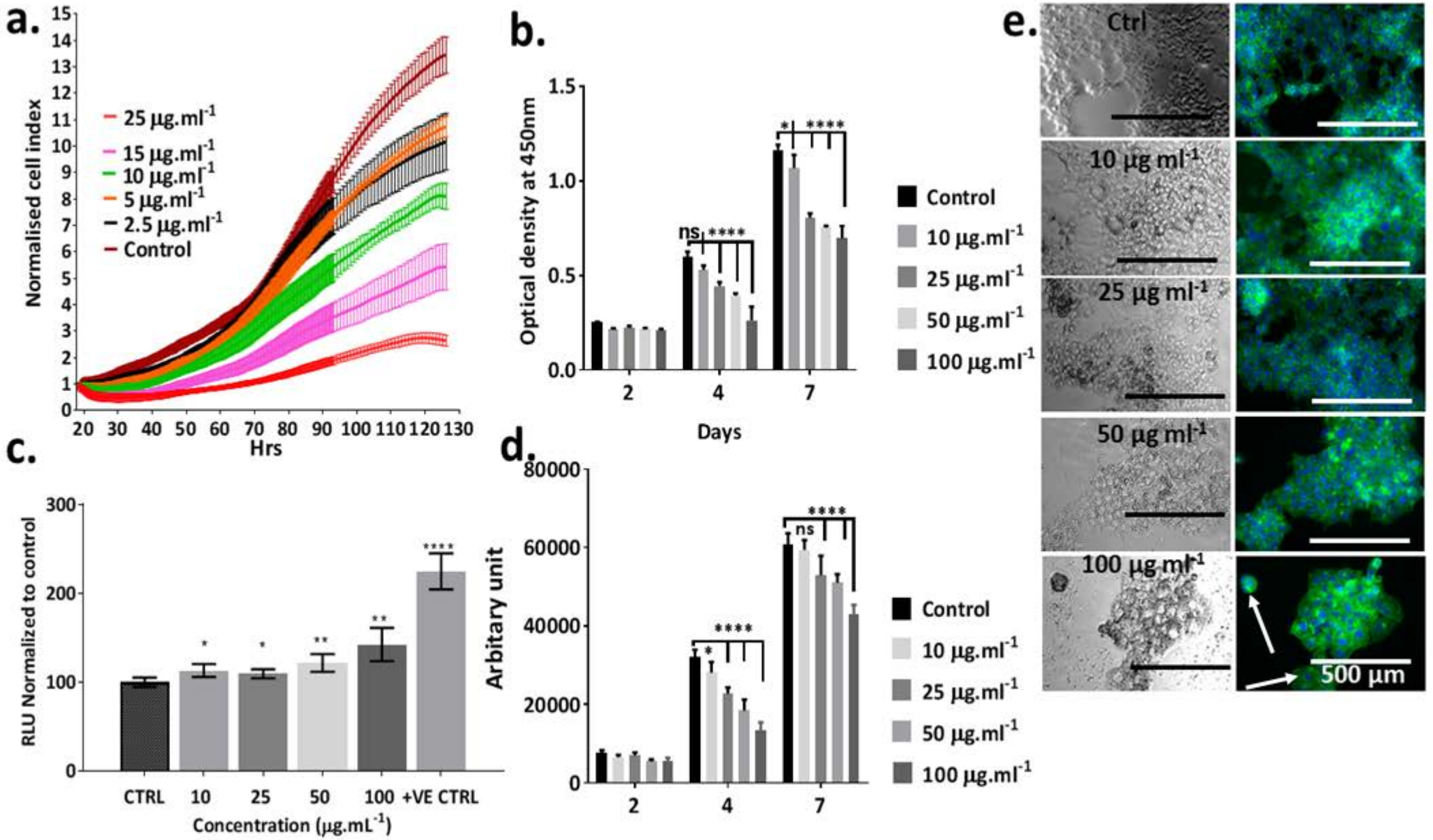
a.
Normalised cell index
Hrs
25 µg.ml-1
15 µg.ml-1
10 µg.ml-1
5 µg.ml-1
2.5 µg.ml-1
Control
b.
Optical density at 450nm
Days
ns
****
*
Control
10 µg.ml-1
25 µg.ml-1
50 µg.ml-1
100 µg.ml-1
c.
RLU Normalized to control
CTRL
10
25
50
100
+VE CTRL
Concentration (µg.mL-1)
d.
Arbitary unit
Days
e.
Ctrl
10 µg ml-1
25 µg ml-1
50 µg ml-1
100 µg ml-1
500 µm

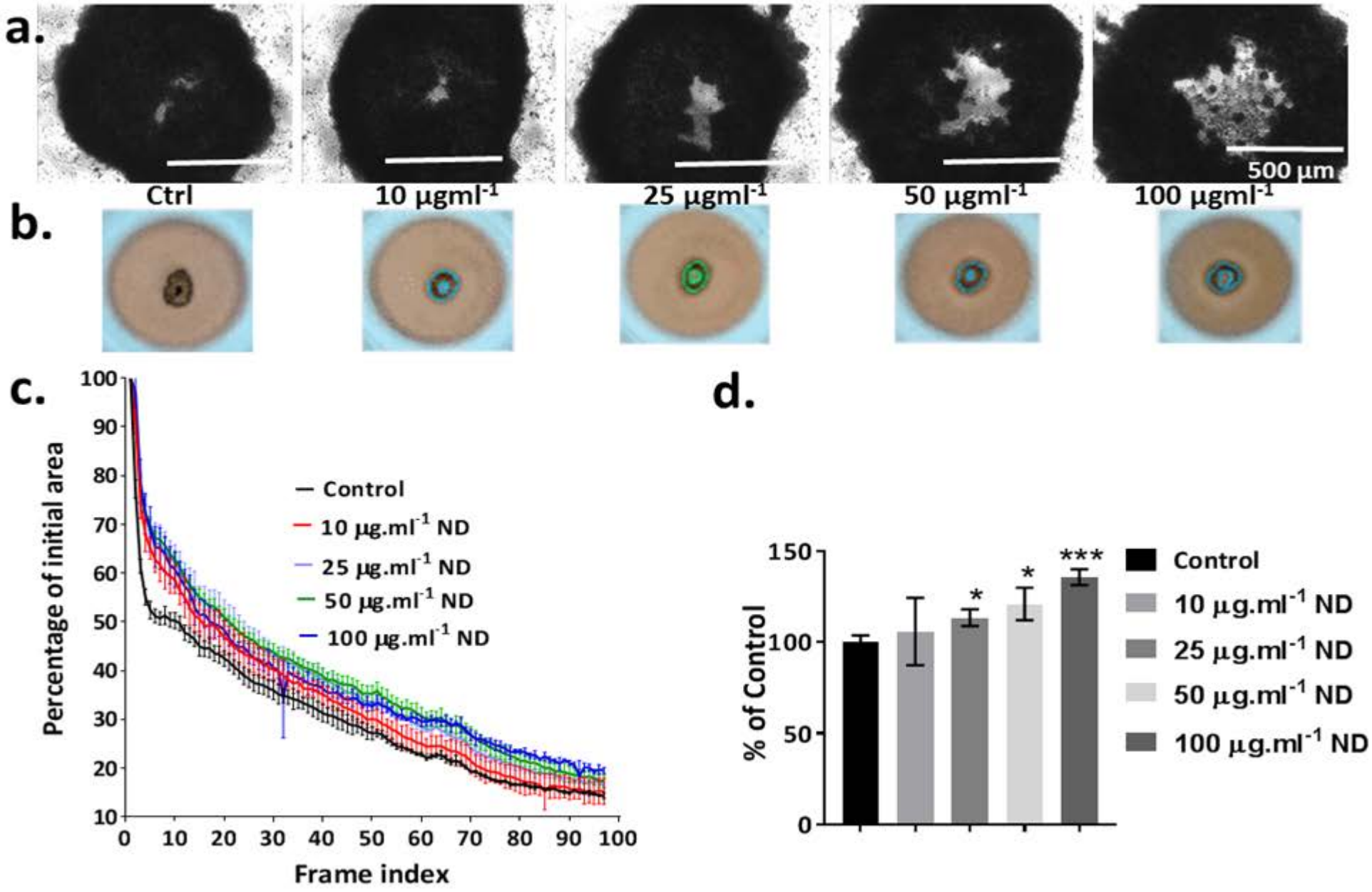
a.
500 µm
Ctrl
10 µgml-1
25 µgml-1
50 µgml-1
100 µgml-1
b.
c.
Percentage of initial area
Frame index
Control
10 µg.ml-1 ND
25 µg.ml-1 ND
50 µg.ml-1 ND
100 µg.ml-1 ND
d.
% of Control
Control
10 µg.ml-1 ND
25 µg.ml-1 ND
50 µg.ml-1 ND
100 µg.ml-1 ND

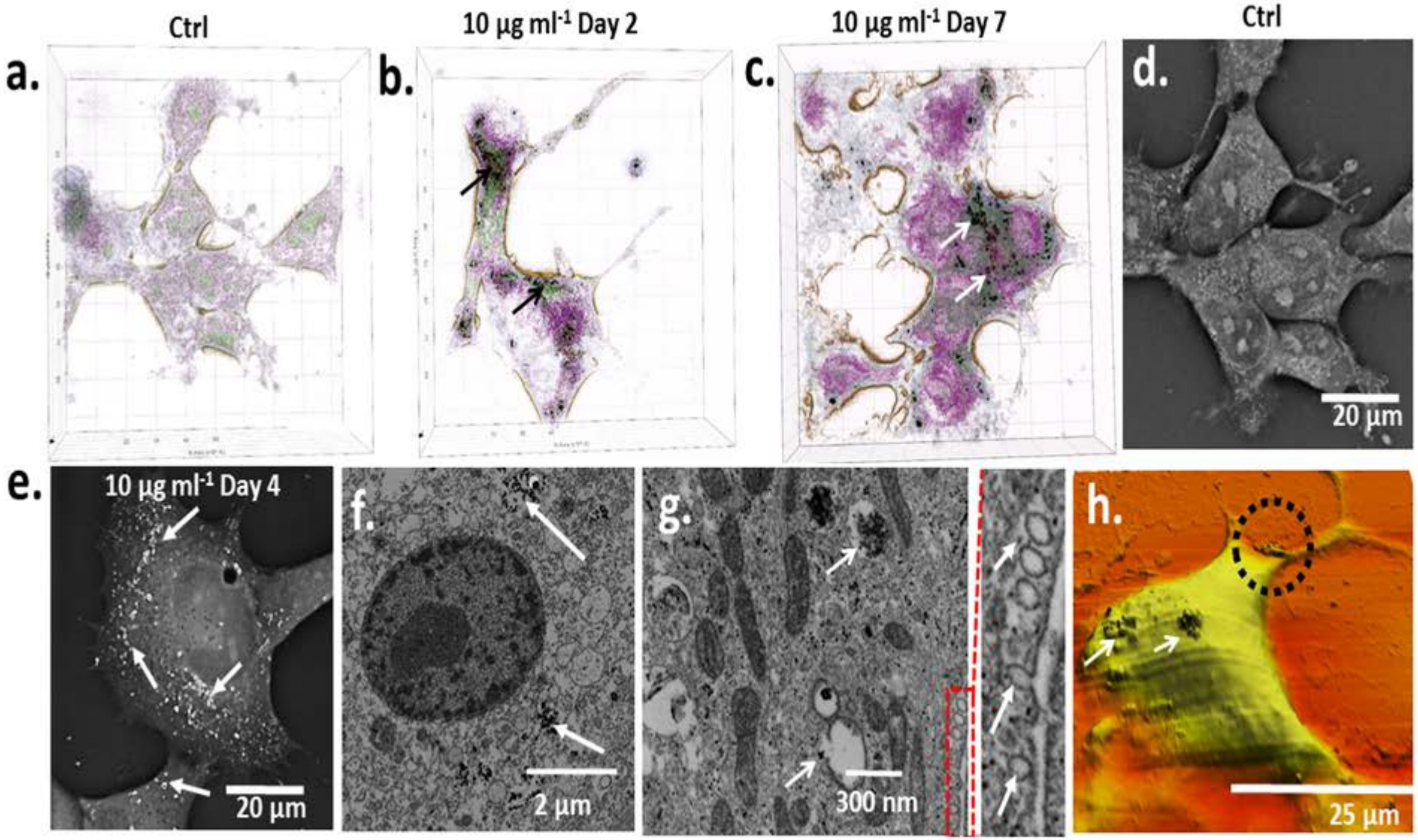
a.
Ctrl
b.
10 µg ml-1 Day 2
c.
10 µg ml-1 Day 7
d.
Ctrl
20 µm
e.
10 µg ml-1 Day 4
20 µm
f.
2 µm
g.
300 nm
h.
25 µm

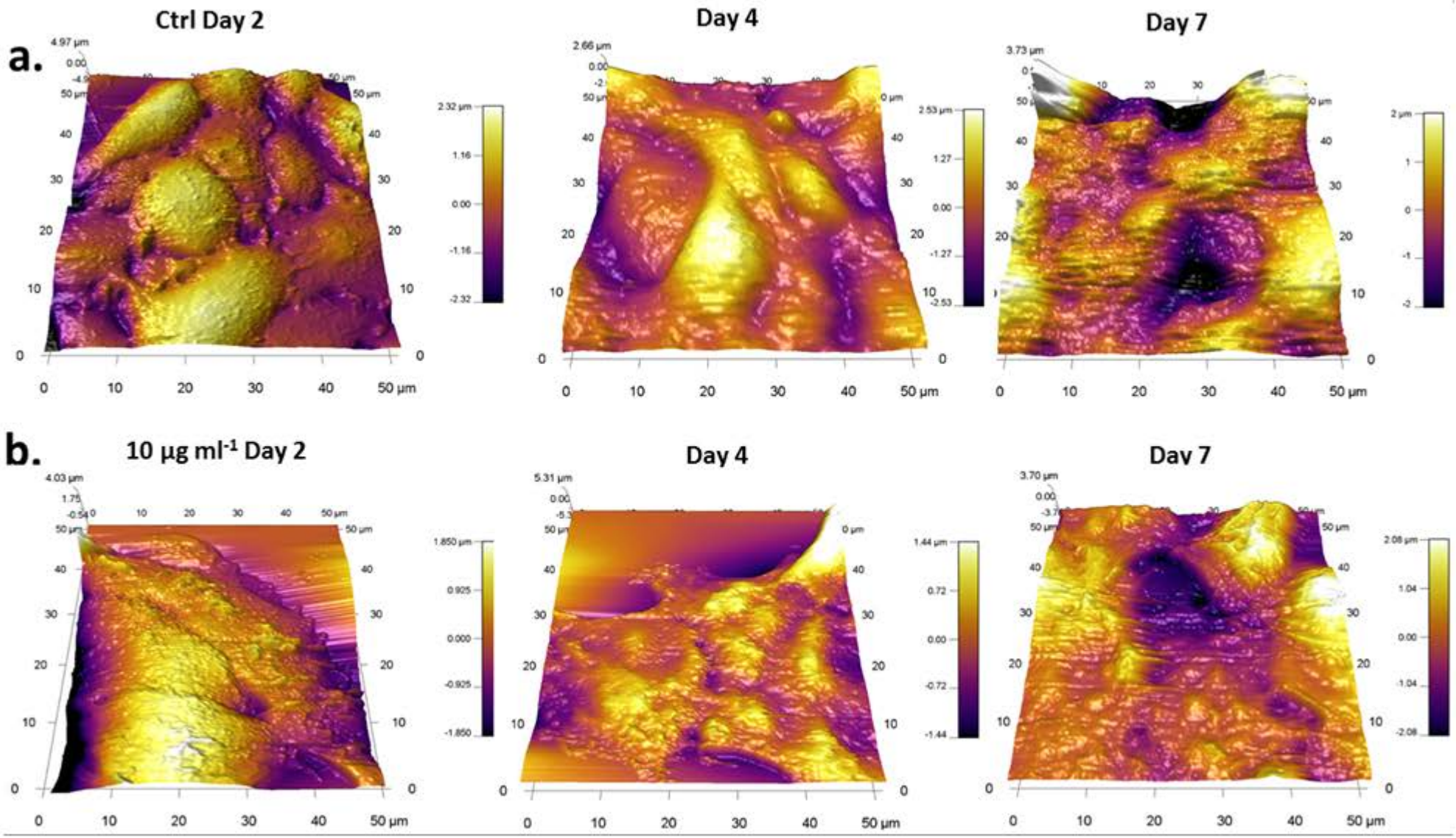
a.
Ctrl Day 2
Day 4
Day 7
b.
10 µg ml-1 Day 2
Day 4
Day 7
0 10 20 30 40 50 µm

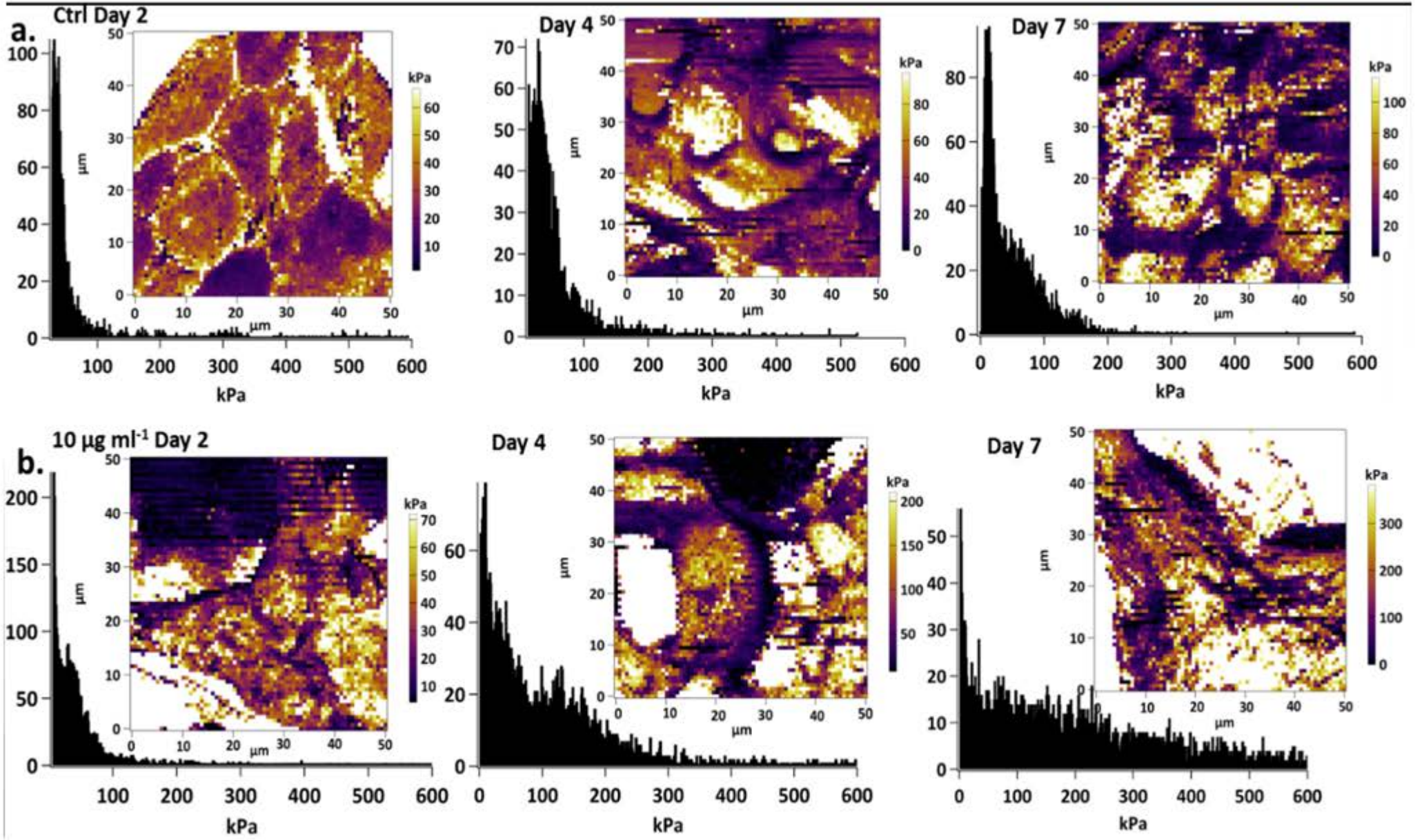
a.
Ctrl Day 2
Day 4
Day 7
b.
10 µg ml-1 Day 2
Day 4
Day 7
kPa
µm

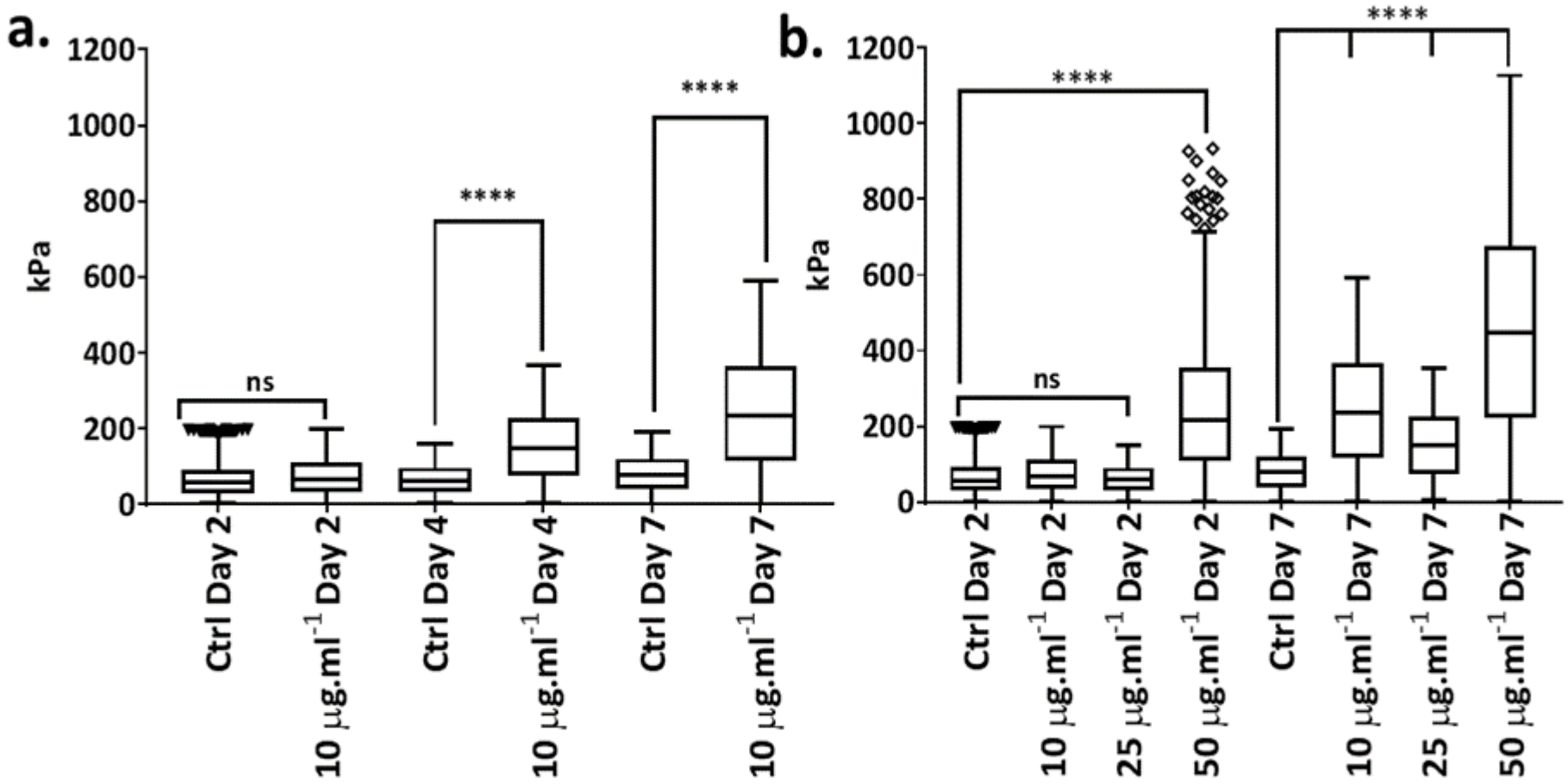
a.
b.
kPa
1200
1000
800
600
400
200
0
ns
****
Ctrl Day 2
10 μg.ml-1 Day 2
25 μg.ml-1 Day 2
50 μg.ml-1 Day 2
Ctrl Day 4
10 μg.ml-1 Day 4
Ctrl Day 7
10 μg.ml-1 Day 7
25 μg.ml-1 Day 7
50 μg.ml-1 Day 7

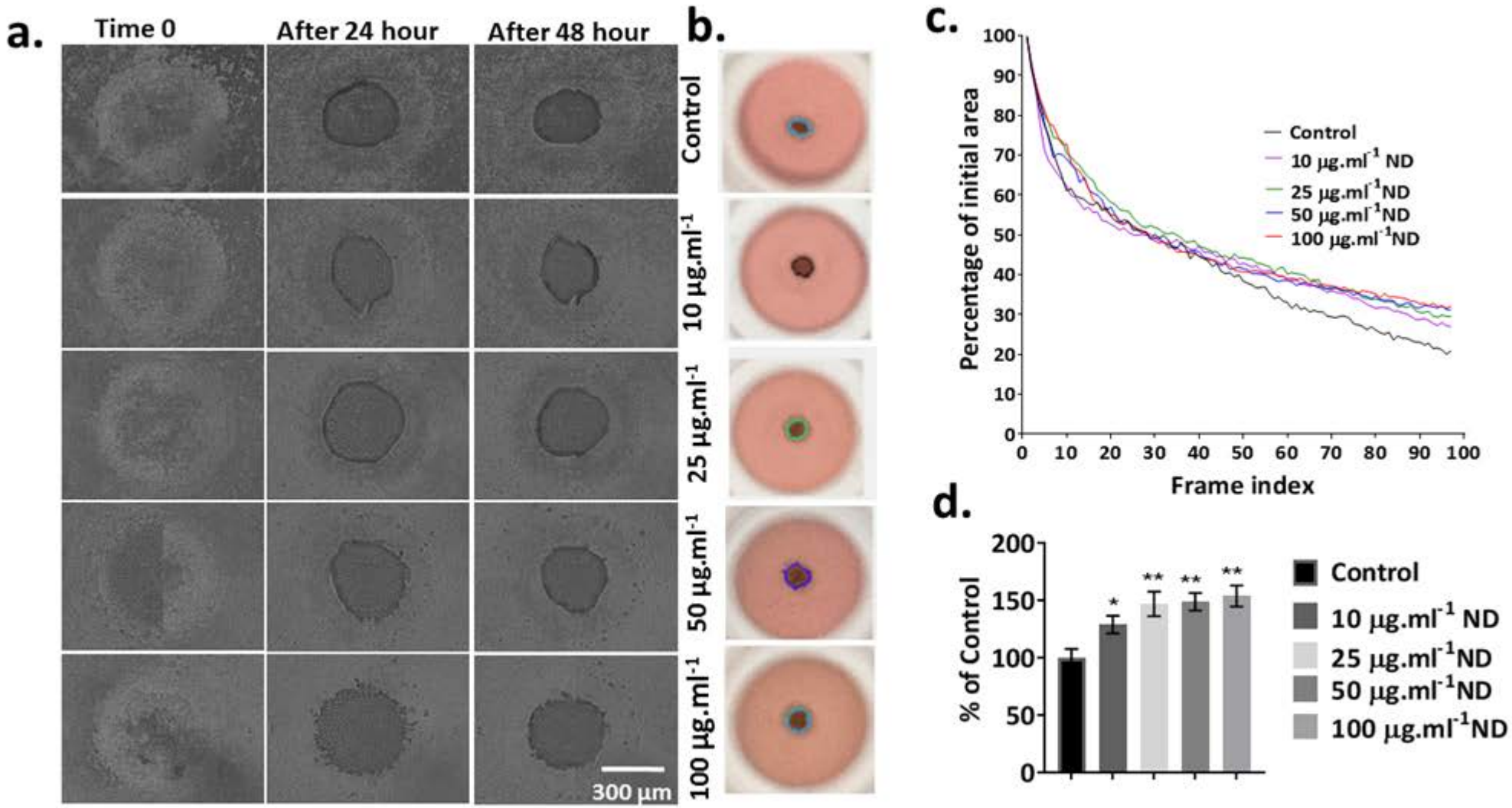
a.
Time 0
After 24 hour
After 48 hour
Control
10 µg.ml-1
25 µg.ml-1
50 µg.ml-1
100 µg.ml-1
300 µm
b.
c.
Percentage of initial area
Frame index
Control
10 µg.ml-1 ND
25 µg.ml-1ND
50 µg.ml-1ND
100 µg.ml-1ND
d.
% of Control
Control
10 µg.ml-1 ND
25 µg.ml-1ND
50 µg.ml-1ND
100 µg.ml-1ND

a.

10 µg ml^{-1} Day 2

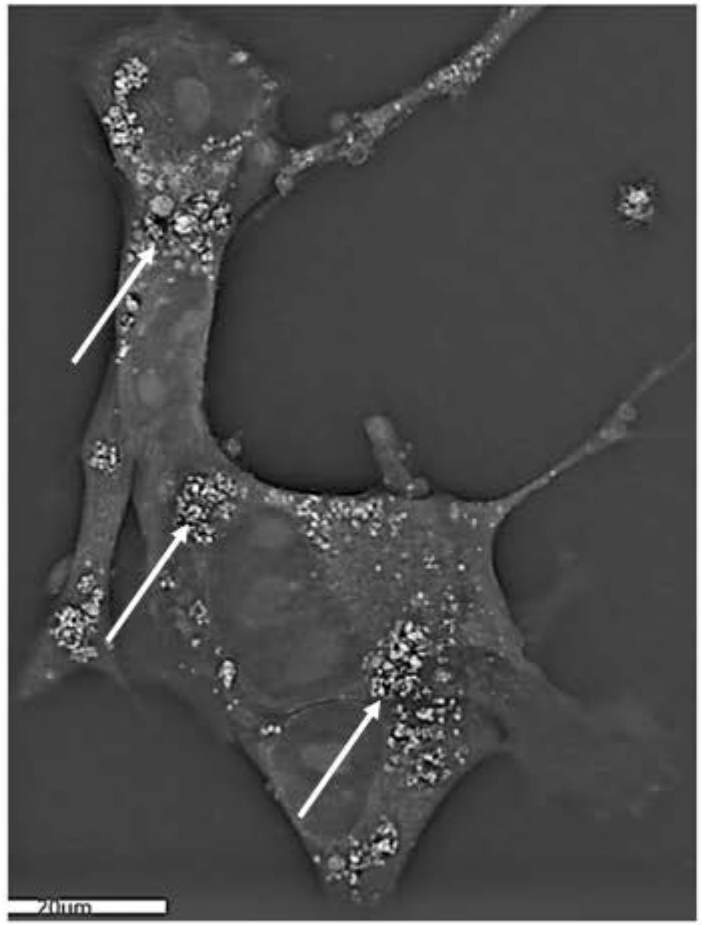

b.

10 µg ml^{-1} Day 7

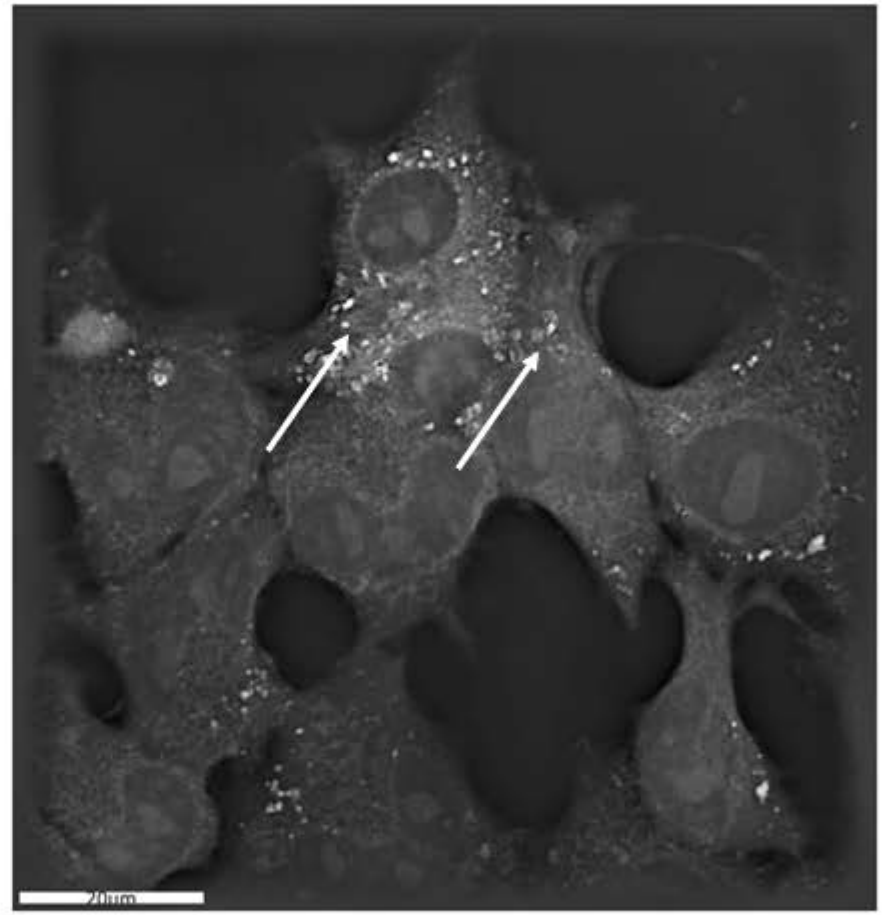

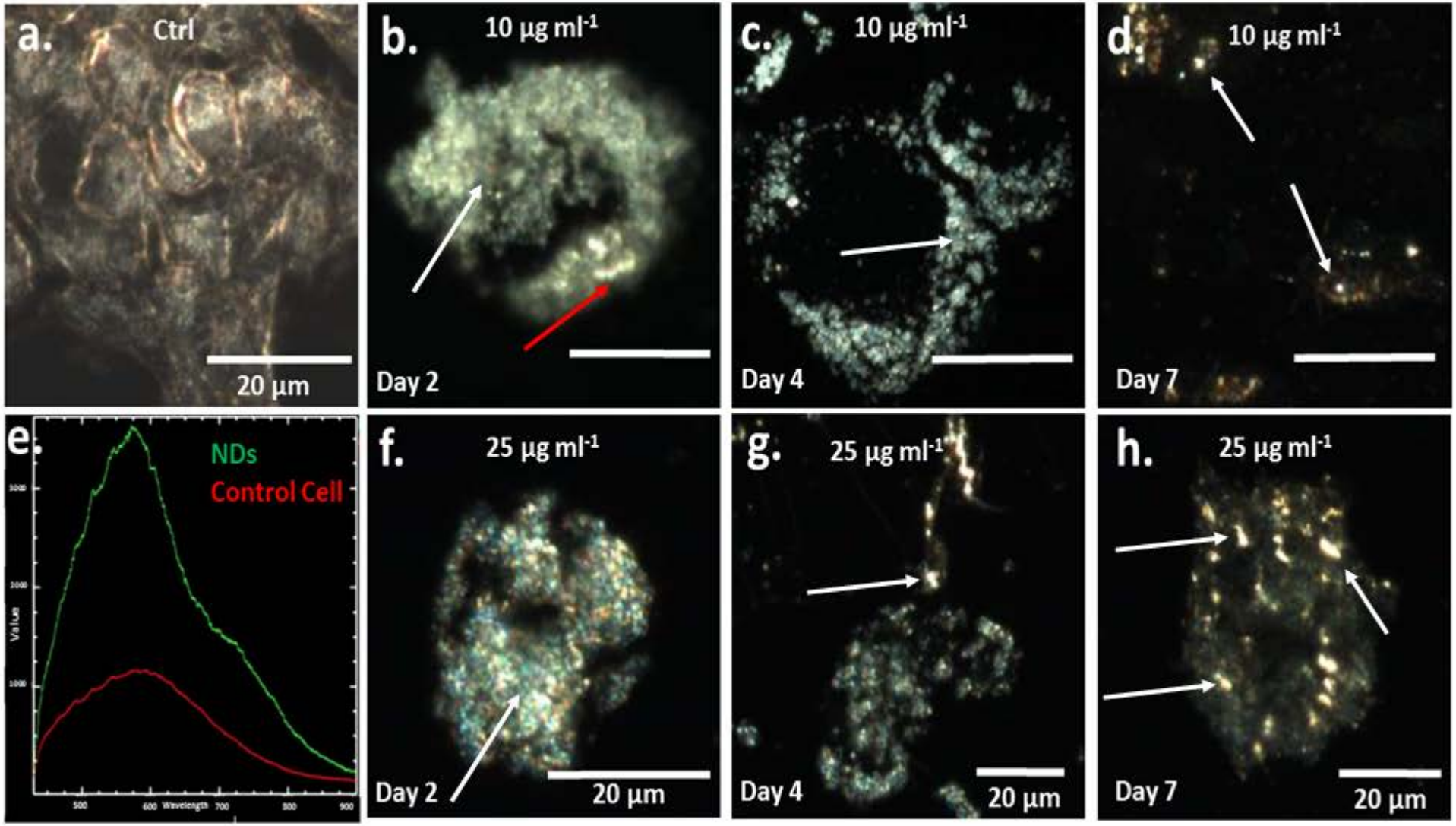
a.
Ctrl
20 µm
b.
10 µg ml-1
Day 2
c.
10 µg ml-1
Day 4
d.
10 µg ml-1
Day 7
e.
NDs
Control Cell
Value
Wavelength
500
600
700
800
900
f.
25 µg ml-1
Day 2
20 µm
g.
25 µg ml-1
Day 4
20 µm
h.
25 µg ml-1
Day 7
20 µm

a.

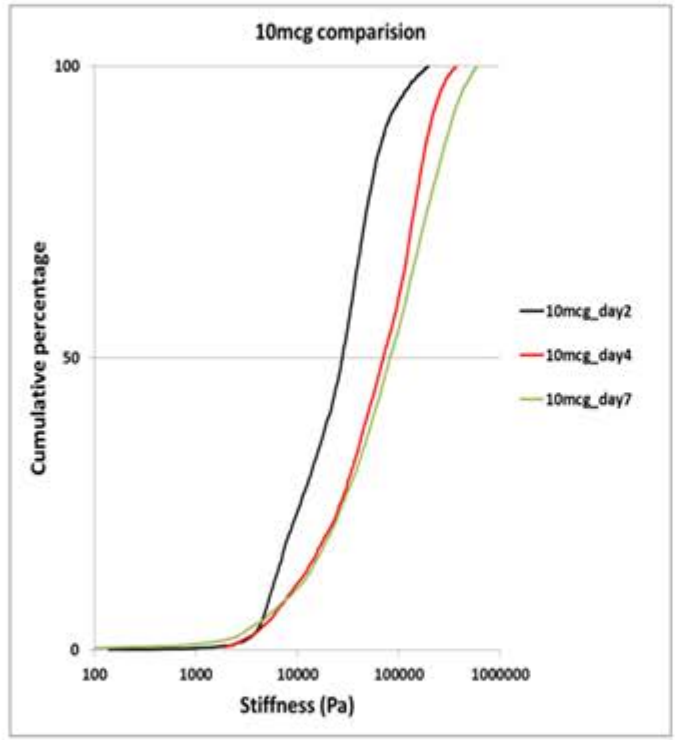
10mcg comparision
100
50
0
Cumulative percentage
100
1000
10000
100000
1000000
Stiffness (Pa)
10mcg_day2
10mcg_day4
10mcg_day7

b.

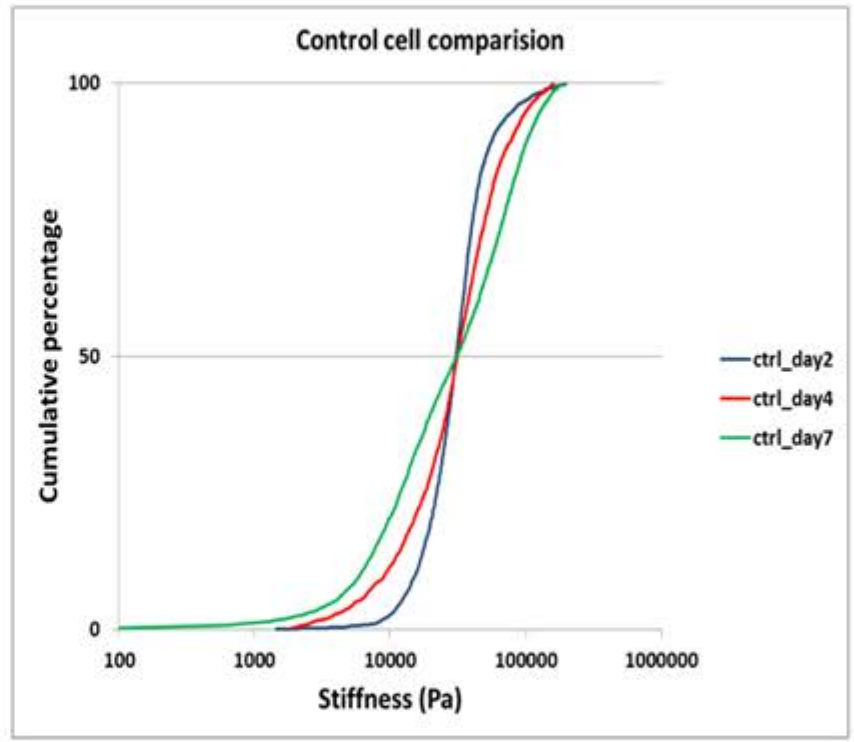
Control cell comparision
100
50
0
Cumulative percentage
100
1000
10000
100000
1000000
Stiffness (Pa)
ctrl_day2
ctrl_day4
ctrl_day7

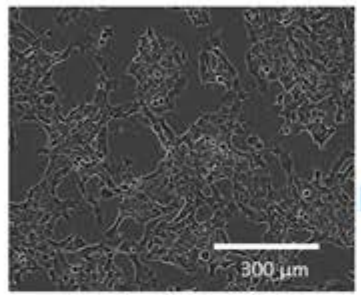

70-80% confluent cells

Magnetize the cells

Levitate the cells with magnet

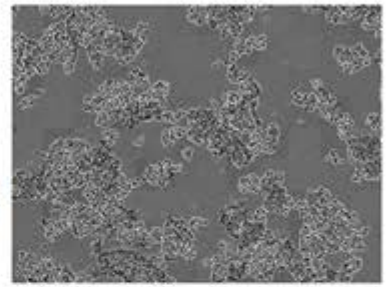

Levitating cells

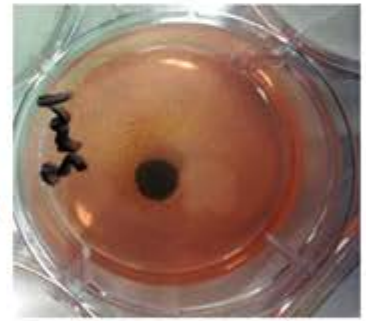

Levitated cluster of cells

Magnetic bioprinting

Bioprinted ring and spheroid

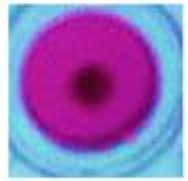

Ipod for live imaging

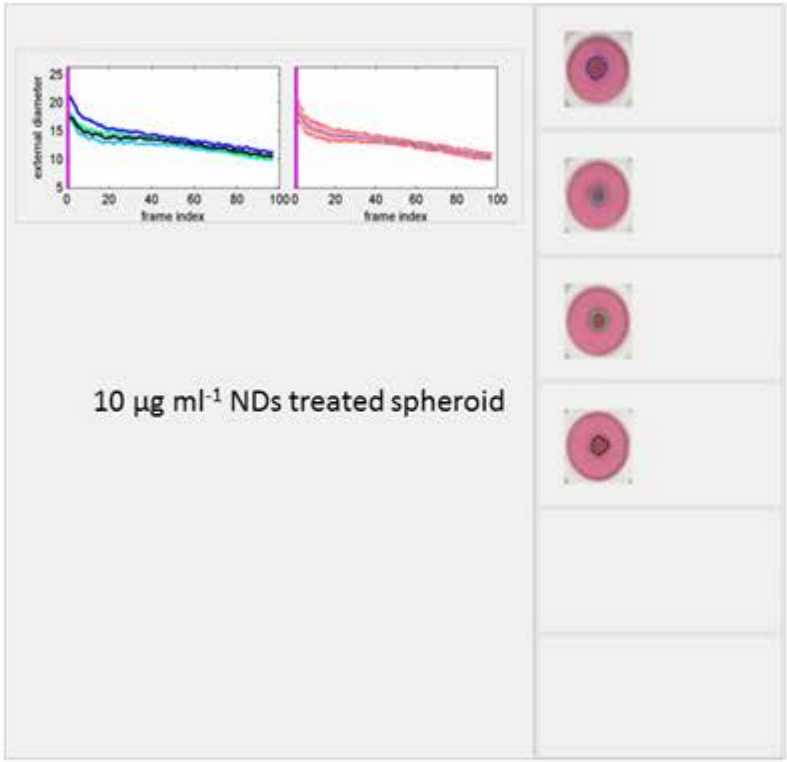

10 µg ml^{-1} NDs treated spheroid

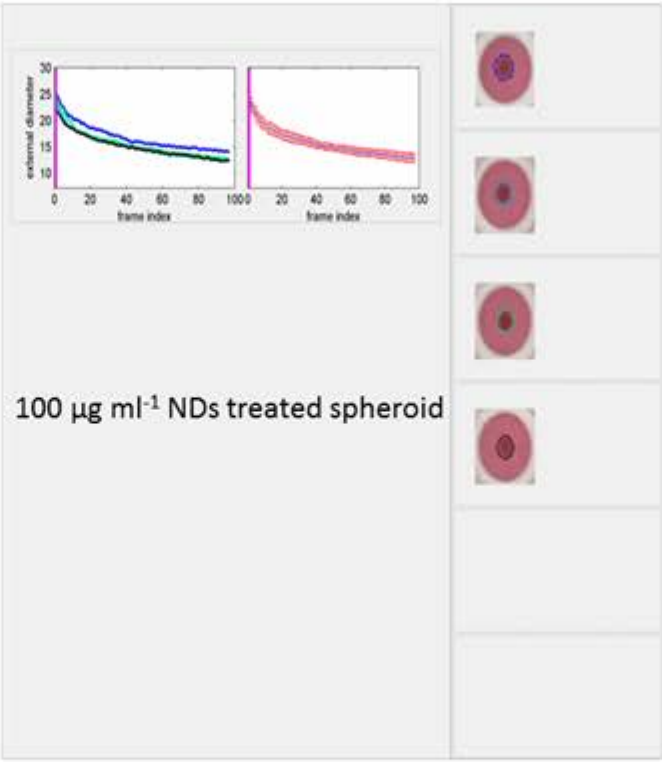

100 µg ml^{-1} NDs treated spheroid

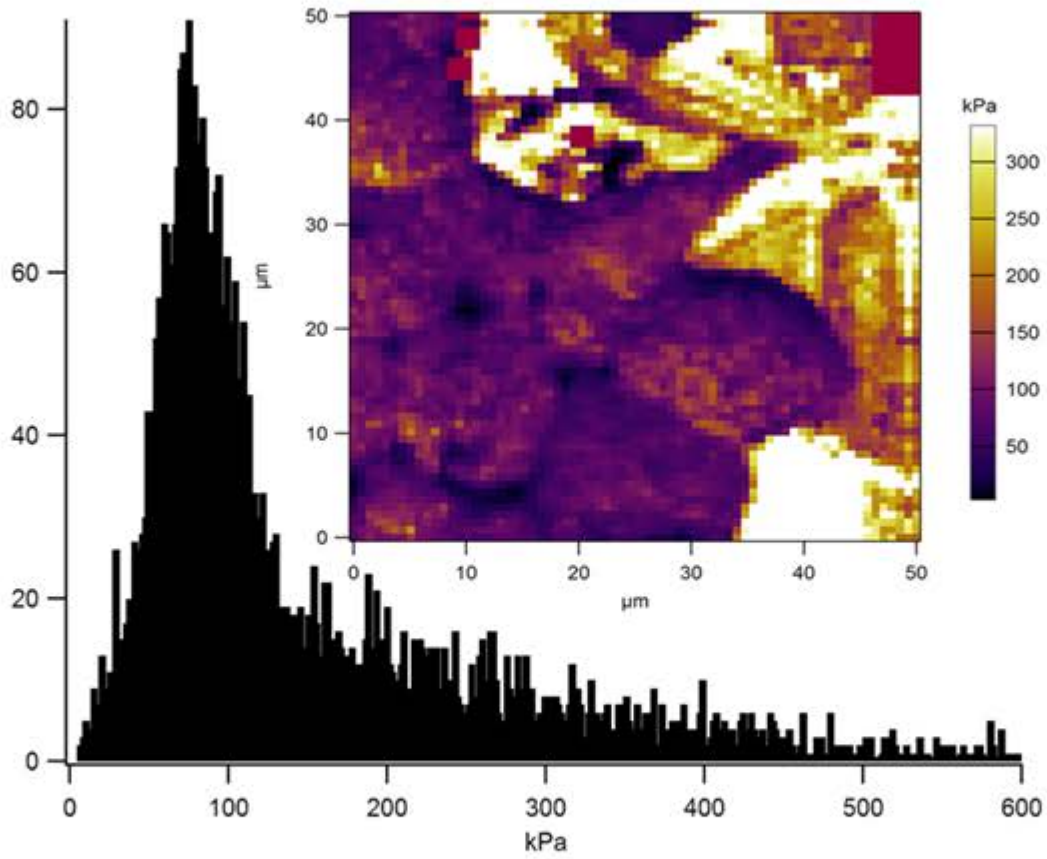
80
60
40
20
0
0
100
200
300
400
500
600
kPa
50
40
30
20
10
0
µm
0
10
20
30
40
50
µm
kPa
300
250
200
150
100
50

Biological impact of nanodiamond particles – label free, high-resolution methods for nanotoxicity assessment.

Dipesh Khanal[1], Fan Zhang[2], Yang Song[3], Herman Hau[1], Archana Gautam[4], Seiji Yamaguchi[5], Jamie Uertz[6], Stewart Mills[6], Alexey Kondyurin[7], Jonathan C. Knowles[8,9,10], George Georgiou[8], Iqbal Ramzan[1], Weidong Cai[3], Kee Woei Ng[4], Wojciech Chrzanowski[1*]

*Correspondence: wojciech.chrzanowski@sydney.edu.au

Methods

Nanoparticle tracking analysis (NTA)

NTA measurements were performed to measure the size distribution of ND dispersion with a Nanosight NS300 (NanoSight, Amesbury, United Kingdom), equipped with a sample chamber with a 488 nm laser. ND dispersion (1 $mg \cdot mL^{-1}$) sonicated for 30 min in DI water was diluted in cell culture medium to a concentration of 5 $\mu g \cdot mL^{-1}$ followed by vortexing for 5 minutes prior to NTA measurements. The advanced script controls options were used for the analysis which comprised of an 80 μL syringe pump driven chamber priming interval, a 30 second pause to minimize vibration artifact, three 60 second video capture periods with constant syringe pump driven sample delivery, and automated laser and pump shutdown after video acquisition. An average of three measurement runs were taken for the data analysis.

Cell viability assays

Fao cells were seeded at a density of 2000 cells/well on 96-well plates and were allowed to attach overnight. Media was aspirated and replaced with particle-conditioned media containing 10, 25,

50 and 100 μg·mL^{-1}. At each predetermined time point (days 2, 4 and 7), cells were washed with PBS once and 100 μL of fresh media containing 10% CCK-8 reagent was added to each well. After three hours of incubation in the dark, the media was transferred to a new 96 well plate, and the optical density (OD) of each well was measured using a microplate reader at 450 nm (Victor x4 multilabel plate reader, Perkin Elmer, USA).

For DNA quantification, media was removed at day 2, 4 and 7 and each well was washed with PBS once followed by addition of 75 μL of Cyquant NF dye reaction mix. Plates were incubated in the dark for 45 min before measuring fluorescence at excitation and emission wavelengths of 485 and 535 nm respectively using microplate reader (Victor X4, multilabel plate reader, Perkin Elmer, USA).

Cytotoxicity of ND in 3D mini-liver model

The effect of NDs on cell growth and function in a 3D environment was quantified using 3D ring closure and dot assays following previously published methodology (Timm, et al., 2013) (Tseng, et al., 2015). In brief, cells were cultured in T-75 flasks and incubated with magnetic nanoparticles (NanoShuttle−PL; Greiner Bio-One, USA) at a concentration of 8 μL.cm^{-2} overnight. After trypsinization magnetized cells were levitated overnight using magnetic drives to form a 'cluster' of cells which were then bioprinted in the shape of rings (2×10^5 cells per ring) and spheroids (1×10^5 cells per spheroid) using a set of magnetic drives. NDs at a concentration of 10, 25, 50 and 100 μg·mL^{-1} were added onto the rings and spheroids (**Fig. S5**). Both internal and external diameters were monitored for 48 h. Images of rings and spheroids were recorded using a mobile device (iPod) and the rate of diameter change (shrinkage and closure of ring), which correlates with the loss of cell function/ mobility, was calculated using a custom-built software Cytox®.

The software embeds the algorithms that can automatically differentiate the foreground (cell) and background (medium) objects from the input video data and compute the diameter(s) of the cell. Briefly, the software takes an input video data, where each frame provides the cell shape at a certain time point. For each frame, the Otsu's method (Otsu, 1979) is used to perform image thresholding to detect the foreground cell regions according to the image pixel information. Next, the contour(s) of the cell is/are detected with morphological processing: an inner contour and an outer contour for ring-shape cell; only an outer contour for dot-shape cell (**Fig. S6**). The diameter of a contour is then computed based on the area of the contour. Therefore, a diameter variation curve is obtained based on the consecutive frames from the input video data. The diameters obtained were used to calculate the areas of both ring and spheroids. These areas were further analyzed to determine the percentage change in area over the 48 h period to estimate IC_{50} concentrations of NDs.

Dark field hyperspectral imaging

Label-free high-resolution hyperspectral imaging was used to investigate the uptake and interaction of NDs with Fao cells which were plated on glass coverslips functionalized using plasma treatment. Each of the coverslips were transferred to a six well plate. Fao cells at a density of 2.5×10^4 cells were plated onto the coverslips and allowed to attach overnight. Next, media was replaced with ND conditioned media at a concentration of 10 and 25 $\mu g \cdot mL^{-1}$ and cells were cultured for up to 7 days. At day 2 and 7 coverslips were taken out and washed with PBS twice followed by fixing with 4% paraformaldehyde (PFA) for 15 min. Fixed cells were washed with PBS three times before mounting onto a glass slide containing fluormount mounting media. Coverslips were sealed with nail polish before dark field hyperspectral imaging using CytoViva

67 microscope (CytoViva, Auburn, AL, USA). The spectra of cells and NDs were obtained and used to
68 identify ND localization within the cells.

69 ***SEM***

70 Fao cells were cultured in complete media on a T75 flask until 70 to 80 % confluency. Media was
71 replaced with media containing 25 $\mu g \cdot mL^{-1}$ of NDs and culture continued for 24 h to allow ND
72 internalization. Next, cells were washed with PBS three times to remove remaining nanoparticles
73 and trypsinised (Tryple™) to collect cells. Cells were transferred to Eppendorf tubes and were
74 centrifuged at 1500 RPM for 5 min to yield cell pellets. Pellets were fixed with 2.5%
75 glutaraldehyde 0.1 M phosphate buffer (pH 7.4) for 15 min followed by post-fixation in 1%
76 osmium tetroxide (OsO_4) in the same buffer. All the samples were further dehydrated with
77 graded ethanol, starting with 30 % to 100 % ethanol. Dehydrated samples were embedded in
78 Spurr's embedding kit (ProScitech, Australia). Ultrathin (70 nm) sections of the cells were the cut
79 on a Leica UltraCut S ultramicrotome (Leica Microsystem GmbH, Vienna, Austria), transferred to
80 formavar coated TEM grids and stained with 2% uranyl acetate and 0.05% aqueous solution of
81 lead citrate. Finally, they were imaged in Gatan back scattered mode with Sigma VP Zeiss field
82 emission SEM maintaining a working distance of 5.1 mm with an electronic high-tension value of
83 1.60 kV.

84 ***Effect of nanodiamond on cytoskeleton***

85 The effect of NDs on cytoskeletal organization was investigated using immunostaining of f-actin.
86 Fao cells were seeded at a density of 2.5×10^3 cells in 2 mL of complete medium in a 6 well plate
87 (Corning, USA). Cells were exposed to NDs at concentrations of 10, 25, 50 and 100 $\mu g \cdot mL^{-1}$ for 4
88 days. At the end of day 4, the media was aspirated, and cells were washed twice with PBS,

followed by fixation with paraformaldehyde (PFA) for 15 minutes. Cells were permeabilised with Triton x for 15 minutes followed by washing with PBS twice followed by staining with Phalloidin CruzFluor 514 for 30 minutes and DAPI 300 nM for 5 minutes (all reagents from Thermo Fisher Scientific). Images were taken using the Nikon eclipse TE2000-U inverted fluorescent microscope.

Fao cell morphology and stiffness measurements

Fao cells were seeded on to plasma treated 50 × 9 mm petri dish (Bacteriological petri dish, Falcon®, Corning, USA) at a density of 5×10^4 cells in 2 mL of complete medium and were allowed to grow overnight. Media was replaced the next day with the ND conditioned media at concentrations of 10, 25 and 50 $\mu g \cdot mL^{-1}$. Cells were exposed to NDs for up to 7 days. At day 2, 4 and 7, media was aspirated and cells were washed with PBS twice followed by fixing with 4% PFA for 15 minutes. Fixed cells were washed with PBS three times and fresh PBS was added to each Petri dish. To investigate the influence of NDs on cell stiffness, cells were probed using Molecular Force Probe (MF3D-Bio, Asylum Research, USA) operating in force-volume mode. The cells were first located using a light microscope and imaged in contact mode using a silicon-nitride cantilever with reflex side gold coating (HYDRA-ALL-G-50, AppNano, CA, USA). Spring constant of each probe was determined using thermal method and were typically around ~65 pN Nm^{-1}. Next, the probe was lowered at a speed of 400 nm s^{-1} onto the cells and cell was indented until the threshold cantilever deflection of 200 nm was reached. The deflection of the cantilever was plotted against the displacement in the z-direction, which gave the force-distance curves. For each sample (control and ND incubated), a minimum of five different cells were scanned and on each sample 50 × 50 μm region was selected for scanning and probing of nanomechanics. For each cell 4900 points were probed (70 × 70 points). Stiffness (apparent elastic modulus, Ea) was

calculated using Hertz model assuming uniform Poisson's ratio of 0.5 (Hertz, 1881). Stiffness values across the surface for all the samples were exported as an array and processed to generate histograms (percent stiffness values within defined bins) as shown in the inserts to stiffness maps shown in **Fig. S4**. Furthermore, the generated data were processed and presented as lognormal cumulative stiffness plots and as box whisker plots to enable statistical analysis and representation of the changes in cell nanomechanical properties.

Supplementary Images

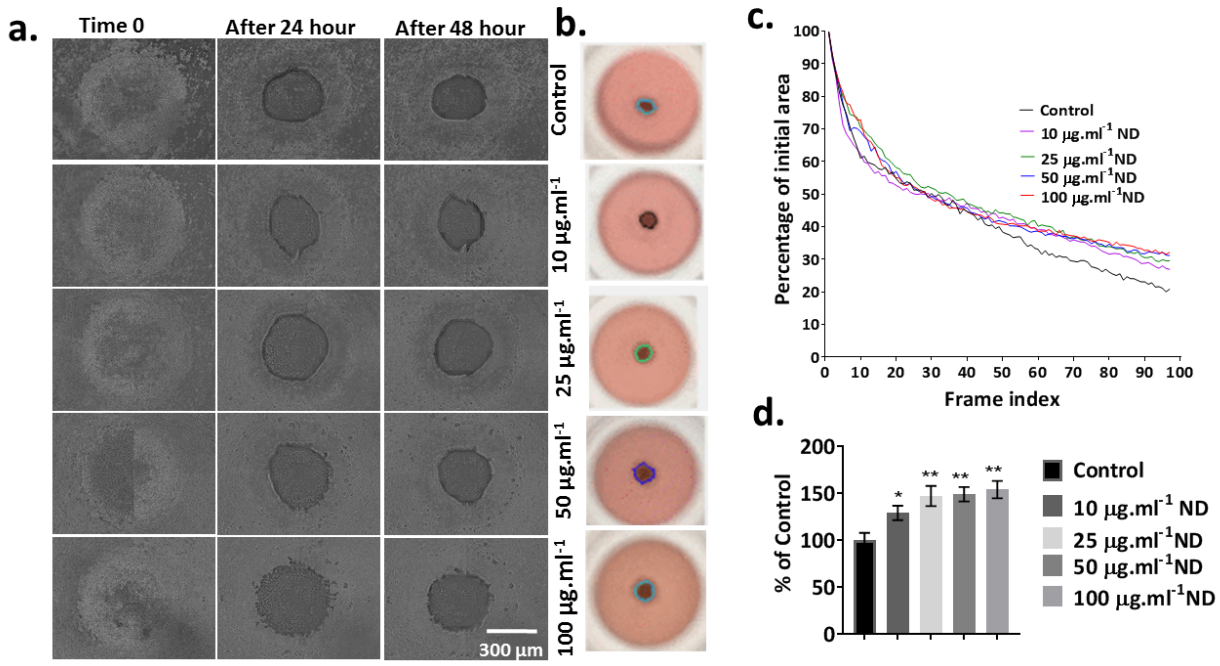

Fig.S1: Spheroid shrinkage assay. (a) Phase contrast image of spheroids exposed to nanodiamond (ND); with increased concentrations of ND, rate of shrinkage decreased significantly. (b) Corresponding images of spheroids along with their contours captured using a mobile device and analyzed by Cytox® software. (c) Graph representing rates of spheroid shrinkage compared to the initial area of the spheroids; increased concentrations of ND led to significant drop in spheroid shrinkage confirming concentration-dependent toxicity of ND. (d) Comparison of spheroid area at the end point of experiment (48 h) confirmed that spheroids exposed to ND had significantly larger area than control spheroids (data presented as mean ± SD, student t-test was used for statistical analysis taking *p<0.05 as significant difference).

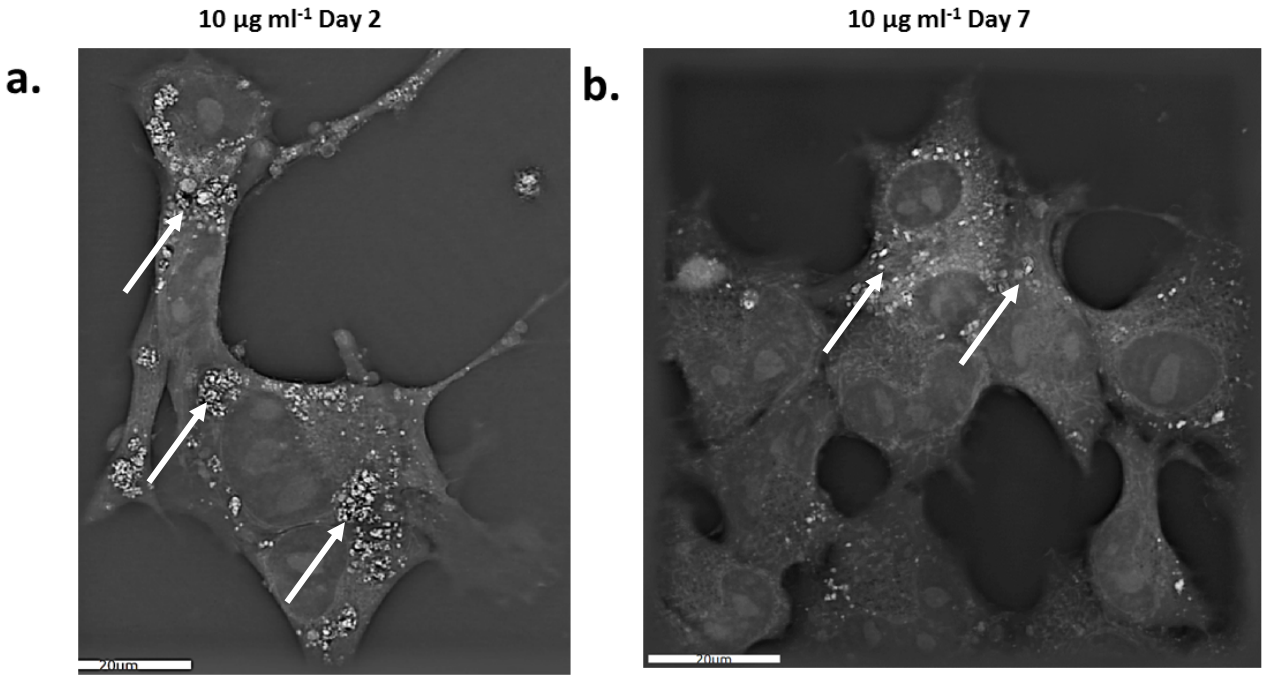

Fig.S2: Unstained holographic tomography images of cells treated with nanodiamond (ND) at day LHS at 2 and RHS at day 7 of exposure. (a) ND (white arrows) are distributed on the surface as well as are internalized. (b) At day 7 lower number of ND (white arrows) can be observed inside the cell possibly due to exocytosis of ND.

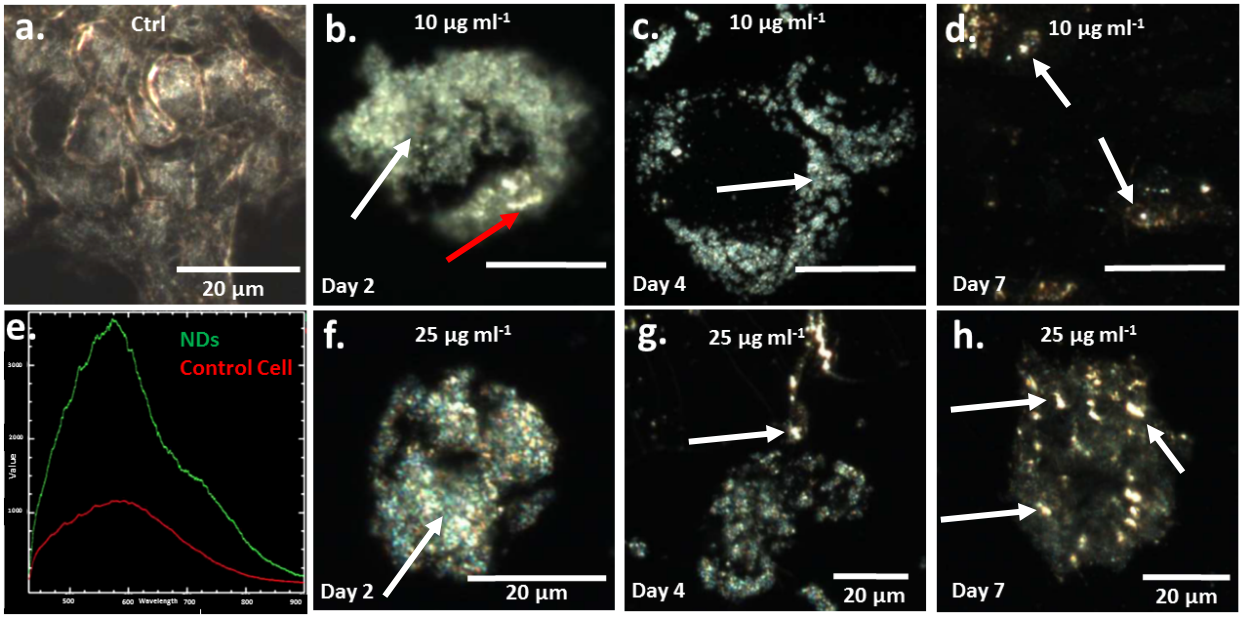

Fig.S3: Dark field hyperspectral imaging of cells before and after exposure to NDs. (a) Control cells show typical morphology of cell with distinct intracellular membrane structures. (b) Cell exposed to ND (10 µg·mL^{-1}) at day 2 showing the presence of majority of ND on the surface of cell (white arrow) with few internalized ND (red arrows). (c) Cell exposed to ND for 4 days show more ND internalized (white arrows). (d) At day 7 few internalized ND can be visualized inside the cell (white arrow). (e) Spectra collected from NDs and control cell show clear difference in refractive index confirming the presence of ND in the cells (f to h). Cells exposed to 25 µg·mL^{-1} for days 2, 4 and 7, show similar trends to the cells exposed to 10 µg·mL^{-1}

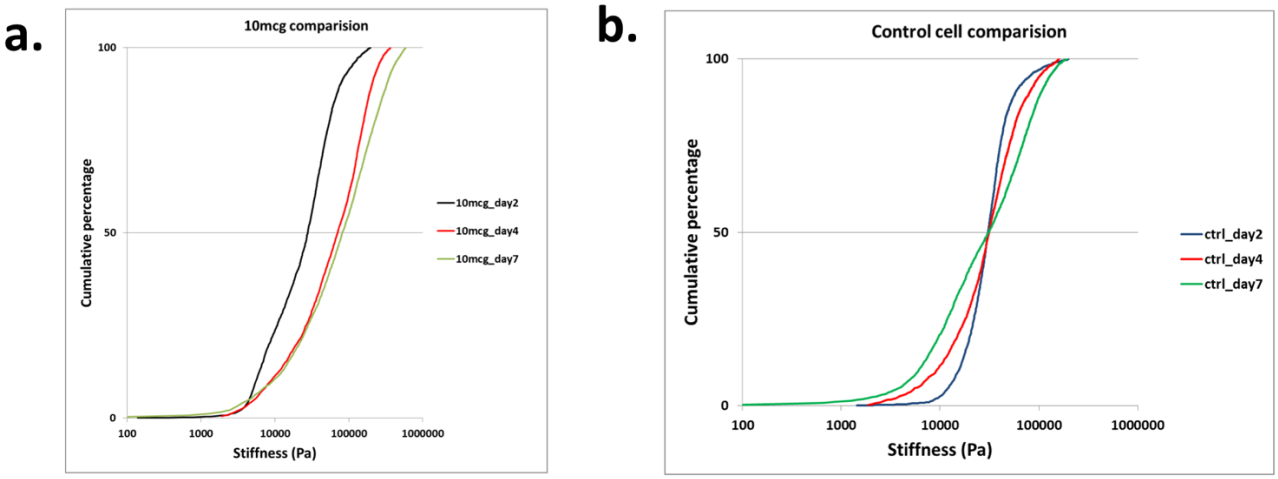

148

Fig.S4: Log-normal cumulative stiffness plots. (a) Cells exposed to ND showed duration-dependent shift in stiffness. (b) Control cells had no significant shift in apparent Young's modulus with longer exposure.

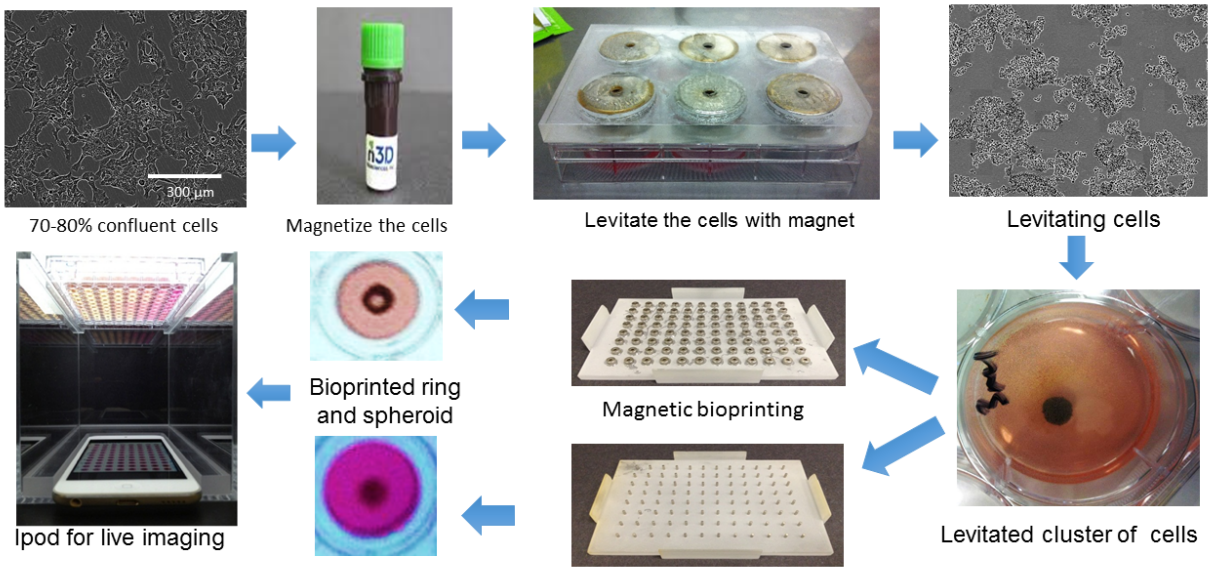

Fig.S5: Schematic for fabricating magnetically bioprinted 3D liver rings and spheroid model and set-up of mobile device for imaging of the rings and spheroids for assessment of toxic effect of nanodiamond.

149

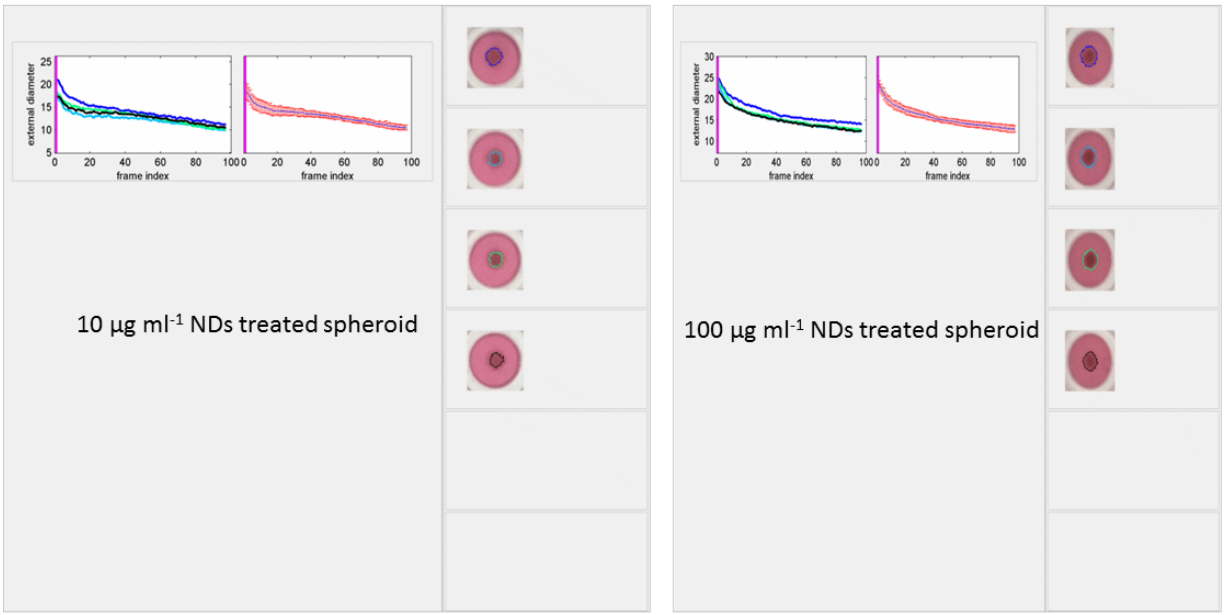

Fig.S6: Evaluation of spheroid shrinkage with custom build Cytox® software

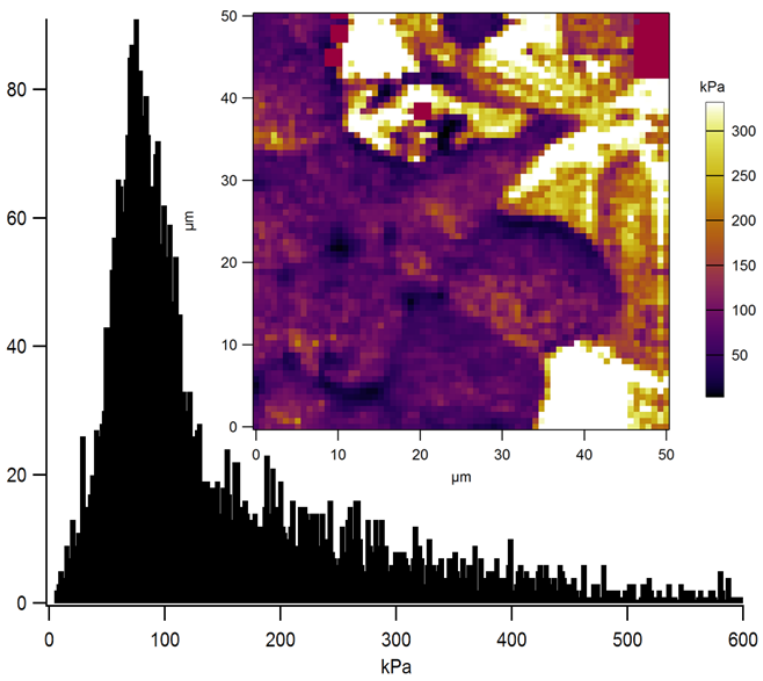

Fig.S7: Distribution of stiffness; apparent Young's modulus maps of Fao cells after exposure to 25 µg·mL^{-1} of NDs nanodiamond (ND): maps for cell exposed to 25 µg·mL^{-1} of NDs confirmed shift in the cell stiffness after exposure to NDs for 48 h (day 2).

150

151